Geophysical Journal International

Geophys. J. Int. (2010) **182,** 1105–1123 doi: 10.1111/j.1365-246X.2010.04673.x

Constraints on deformation mechanisms during folding provided by rock physical properties: a case study at Sheep Mountain anticline (Wyoming, USA)

K. Amrouch,[1,2,3]* P. Robion,[4] J.-P. Callot,[1] O. Lacombe,[2,3] J.-M. Daniel,[1] N. Bellahsen[2,3] and J.-L. Faure[1]

[1]*Geology Geochemistry Geophysics Direction, Institut Français du Pétrole, Rueil-Malmaison, France. E-mail: khalid.amrouch@gmail.com*
[2]*UPMC Univ Paris* 06, *UMR* 7193, *ISTEP, F-*75005, *Paris, France*
[3]*CNRS, UMR* 7193, *ISTEP, F-*75005, *Paris, France*
[4]*Département Géosciences et Environnement, Université de Cergy-Pontoise,* 95031 *Cergy-Pontoise, France*

Accepted 2010 May 20. Received 2010 May 18; in original form 2009 October 19

SUMMARY

The Sheep Mountain anticline (Wyoming, USA) is a well-exposed asymmetric, basement-cored anticline that formed during the Laramide orogeny in the early Tertiary. In order to unravel the history of strain during folding, we carried out combined anisotropy of magnetic susceptibility (AMS), anisotropy of *P*-wave velocity (APWV) and Fry strain analyses. The results are compared to previously published stress–strain data from calcite twins at the microscopic scale and from fracture sets at the mesoscopic scale, and are used to discuss the kinematics and mechanics of forced folding. The results obtained in sandstone and carbonate lithologies demonstrate a good agreement between (1) the principal axes of the AMS and APWV tensors, (2) stress–strain tensors derived from calcite twins, (3) Fry strain axes and mesoscopic fracture sets. Furthermore, these tensors are coaxial with the main structural trends of the anticline. The differences between AMS and APWV fabrics on one hand, and the differential stress values of the forelimb and the backlimb on the other hand, emphasize how the macroscopic asymmetry of Sheep Mountain anticline affects the strain pattern at the microscopic scale. The data set presented in this paper offers a consistent mechanical scenario for the development of Sheep Mountain anticline.

Key words: Magnetic fabrics and anisotropy Microstructures; Continental tectonics: compressional; North America.

1 INTRODUCTION

The study of fold evolution is typically based on analytic and numerical models that are used to investigate possible kinematic scenarios of folding, based on the present-day geometry of folded strata and geometrical assumptions such as thickness and length preservation. Dahlstrom (1969), Suppe (1985), Jamison (1987), Chester & Chester (1990), Erslev (1991) and Mitra (2003), for example, have described fold evolution from a kinematic perspective. Although this approach has proven to be useful to propose consistent geometrical models of folding, it is mainly macroscopic, and the successive deformation mechanisms that accommodate internal strain within folded strata at the meso- to microscopic scale remain to be properly linked to such geometrical models.

In addition to regional-scale thrust faults and folds, it is well known that tectonic shortening in foreland fold-thrust belts generates fracture sets and faults at the mesoscale, and pressure-solution cleavage and grain-scale deformation (e.g. mechanical compaction, twinning in calcite grains) at the microscale. Pressure-solution processes and grain-scale deformation begin early during the deformation history and are related to burial compaction and layer-parallel shortening (LPS) (e.g. Roure *et al.* 2005). The mechanisms active during the LPS stage have been described in detail in recent years for sandstone rocks (Frizon de Lamotte *et al.* 2002; Saint-Bezar *et al.* 2002; Sans *et al.* 2003; Robion *et al.* 2007) as well as for carbonate rocks (Evans *et al.* 2003; Marfil *et al.* 2005; Evans & Elmore 2006; Graham 2006). However, while the appraisal of the mechanical behaviour of folded strata is an essential aspect to understand and simulate the evolution of folded/faulted formations, only a few

*Now at: UMR 7193, ISTEP Institut des Sciences de la Terre de Paris, Campus Jussieu – Tour 46-45, 2ème étage, boîte courrier 129, 4, Place Jussieu, 75252, Paris Cedex 05, France.

attempts have been made to bridge the gap between the macroscopic scale and the microscopic scale (Frizon de Lamotte *et al.* 1997; Parés & Van der Pluijm 2002; Evans *et al.* 2003; Louis *et al.* 2006). This paper aims at unraveling the history of strain acquisition and at linking macroscale and microscale mechanisms of deformation active during folding. The underlying question is to what extent structural observations made at the microscopic scale may be related to the fold scale, and vice versa. The chosen case study is the Sheep Mountain anticline (Erslev 1993; Bellahsen *et al.* 2006a,b; Amrouch *et al.* 2010), a well-exposed Laramide basement-cored anticline in Wyoming (USA). This work focuses on the description and characterization of small-scale deformation by combining various techniques of microstructural analysis: anisotropy of magnetic susceptibility (AMS hereinafter), anisotropy of *P*-wave velocity (APWV hereinafter) and Fry strain analysis. The results of this study are compared to stress–strain patterns previously reconstructed from fractures and calcite twins (Bellahsen *et al.* 2006a; Amrouch *et al.* 2010) in order to decipher the relative contribution of fracturing and of matrix deformation in the accommodation of internal strain of strata during folding. This paper demonstrates how the combination of these various approaches can help to characterize the succession of microscopic deformation mechanisms active during folding of sedimentary rocks (i.e. compaction, intragranular and transgranular fracturing and pressure-solution).

2 GEOLOGICAL SETTING

The Sheep Mountain anticline is located on the eastern edge of the Bighorn Basin, Wyoming (Fig. 1). It is a NW–SE trending, asymmetric basement-cored fold that formed above a SW dipping high angle thrust fault during the Laramide orogeny and under a regional NE–SW compression (Hennier & Spang 1983; Engebretson *et al.* 1985; Forster *et al.* 1996; Bird 2002; Stanton & Erslev 2004). The Bighorn River cuts the anticline normal to the fold axis, providing excellent exposure of the stratigraphic section of the fold core. Bedding dips are between 10° and 40° to the SW in the backlimb and can be locally overturned in the forelimb. NE of the anticline, the Mesozoic rocks are folded with fold trends oblique to the main Bighorn trend, being probably detached from the Palaeozoic sequence and basement above the Triassic Chugwater shales.

The outcropping Palaeozoic sedimentary sequence in the Bighorn Basin is approximately 3 km thick (Hennier & Spang 1983; Rioux 1994; Forster *et al.* 1996). Fig. 2 shows the formations that crop out at Sheep Mountain anticline. The oldest exposed unit is the Lower Mississippian Madison limestones, which are approximately 230 m thick. Above this unit, the Mississippian Amsden formation (35 m thick) consists of crossbedded quartz arenites, siltstones, sandstones, shales and carbonates. The Amsden formation is overlain first by sandstones, shales and carbonates topped by quartz arenites of the Upper Mississippian Tensleep formation (29 m thick). Above, the 70 m thick Permian Phosphoria formation is made of predominantly siltstones and shales overlain by thick carbonates. Above these formations lies the Triassic Chugwater formation, the youngest unit exposed at Sheep Mountain anticline, which is approximately 170 m thick with sandstones and shales. Given the complexity of this lithologic succession we have chosen to study separately the carbonates (Madison and Phosphoria formations) and the sandstones (Tensleep and Amsden formations) sandwiched in between.

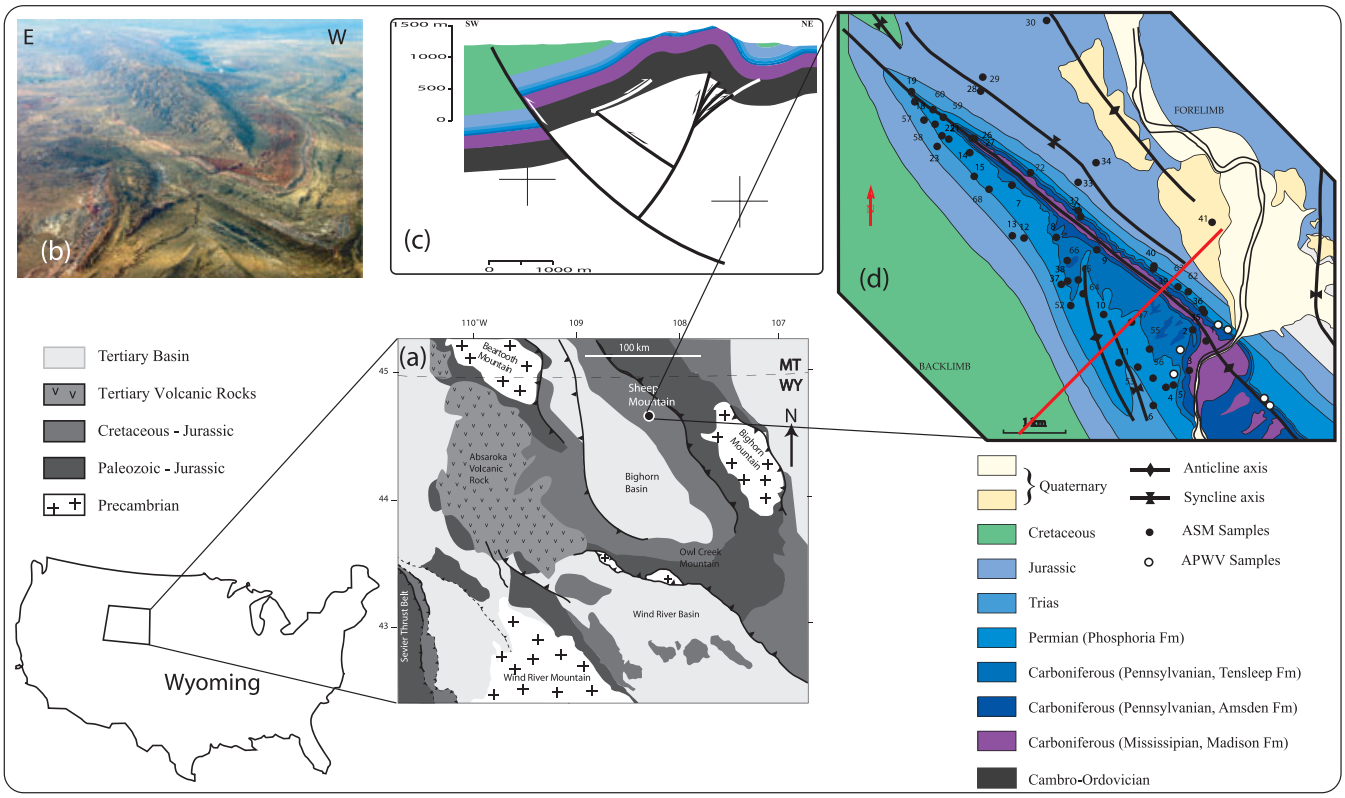

Figure 1. (a) Simplified geological map of the Wyoming state. (b) Aerial photograph of Sheep Mountain anticline (view from the NNW); (c) Geological cross-section through of Sheep Mountain anticline perpendicular to the strike of the average fold axis (after Amrouch *et al*. 2010) and (d) Geological map of study area of SMA (after Rioux 1994).

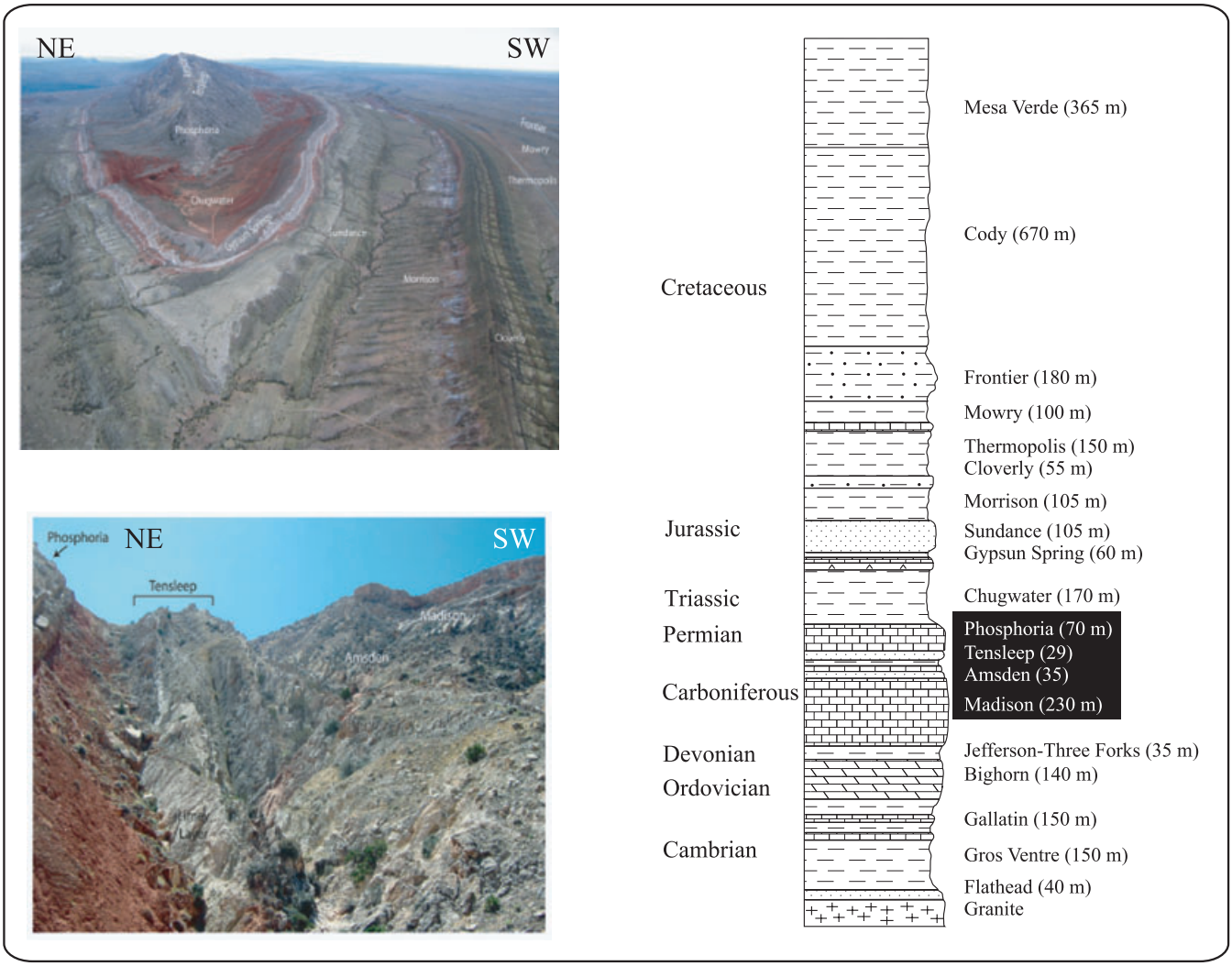

Figure 2. Stratigraphic column of sedimentary formations exposed at SMA. Formation thicknesses are based on published sections (Ladd 1979). Aerial (top panel) and field (bottom panel) pictures showing the various formations cropping out in Sheep Mountain anticline.

Based on orientation, deformation mode and crosscutting relationships, four main successive joint sets were identified in Sheep Mountain anticline (sets I to IV, Bellahsen *et al.* 2006a; Fiore 2006; Amrouch *et al.* 2010). Set I joints strike 110° to 130° (after unfolding), slightly oblique to the fold trend; this early set is interpreted as a regional fracture set that predates the Laramide orogeny (e.g. Bellahsen *et al.* 2006a; Amrouch *et al.* 2010). Set II joints striking 045° (after unfolding) and observed mainly in the hinge and the backlimb are interpreted as related to the NE-oriented Laramide compression (Dickinson and Snyder 1978; Engebretson *et al.* 1985; Bird 2002; Bellahsen *et al.* 2006a; Amrouch *et al.* 2010) just prior to and during initial anticline growth (i.e. LPS related joints). A dense set of joints striking 135° (Set III), parallel to the fold axis, is found mainly along the hinge line. It is interpreted as having formed in response to bending stresses during folding. Set IV joints are vertical and strike 110° (in their current position); they may have developed in the backlimb in response to stress release during fold exhumation. Bedding-parallel slip, evidenced by slickensides along bedding surfaces in the Madison formation, tail cracks emanating from bedding surfaces in the Phosphoria formation, and polished bedding surfaces of the Phosphoria formation indicates that flexural-slip with slip directions approximately normal to the fold axis (Hennier & Spang 1983; Sanz *et al.* 2008) partly accommodates shortening.

3 METHODOLOGY AND SAMPLING

One objective of this study is to characterize properly the internal deformation of carbonates and sandstones during folding. To achieve this objective, we carried out a study of AMS, APWV and Fry strain analysis, because the combination of these techniques has proven to be very efficient to describe the microscale deformation of rock samples (e.g. Louis *et al.* 2006; Burmeister *et al.* 2009; Soto *et al*. 2009). The remarkable exposure of the strata and the small size of the Sheep Mountain anticline allow making a rather complete collection of samples from all locations within the fold, that is, in both limbs and hinge.

The anisotropic behaviour of sedimentary rocks with respect to a particular physical property (elasticity, magnetic susceptibility, electrical conductivity and permeability) is determined by both matrix properties and pore space distributions (Lo *et al.* 1986). Such information is of importance for inferring the microstructural characteristics and understanding the weak deformations in sedimentary

rocks (Louis *et al.* 2003). The matrix of a sedimentary rock can be anisotropic, for instance, because of preferred mineral orientation, water currents during deposition or pressure solution in response to an anisotropic stress field during loading. The pore space distribution can be anisotropic because of the sedimentation processes controlled by gravity, which often result in transversely isotropic rocks, depositional processes driven by water currents, and the presence of preferentially oriented cracks within or between the minerals. In the latter case, the cracks appear mainly to follow non-isotropic stress conditions or loading/unloading episodes (Louis *et al.* 2003).

We have used three parameters to characterize the magnitude and the shape of the measured AMS and APWV tensors: (i) the corrected degree of anisotropy P_j of Jelinek (1981) ranging from 1 (sphere) to infinity characterizes the ellipticity and can be written as $P_j = \exp\sqrt{2[(\eta_1-\eta)^2+(\eta_2-\eta)^2+(\eta_3-\eta)^2]}$ where η_1, η_2 and $\eta_3$are the natural logarithms of the tensor eigenvalues and $\eta = (\eta_1+\eta_2+\eta_3)/3$, (ii) the shape parameter T ($T = (2\eta_2-\eta_1-\eta_3)/(\eta_1-\eta_3)$), and (iii) the mean of the eigenvalues $A_m = (A_1+A_2+A_3)/3$; $A =$ *K or V*, where K is the magnetic susceptibility and V is the P wave velocity.

3.1 AMS and rock magnetic properties

The measurement of AMS is commonly used for petrofabric and structural studies to characterize weak deformation (e.g. Kissel *et al.* 1986; Hrouda 1991; Averbuch *et al.* 1992; Borradaile & Henry 1997). The measurement of AMS helps to characterize penetrative tectonic fabrics in deformed rocks because AMS is sensitive to even slight preferred orientations of magnetic minerals (e.g. Fuller 1964; Kligfield *et al.* 1977; Rathore 1979; Borradaile & Tarling 1981; Kissel *et al.* 1986; Lowrie & Hirt 1987; Aubourg *et al.* 1991; Borradaile 1991; Averbuch *et al.* 1992; Lüneburg *et al.* 1999; Parés *et al.* 1999). However, whereas the correlation between the orientations of principal AMS axes and principal strain axes tends to be very consistent, the correlation between the magnitudes of principal AMS axes and corresponding principal strain axes is not (e.g. Evans & Elmore 2006; Latta & Anastasio 2007)

Our analysis of AMS was carried out by using a spinner kappabridge KLY-3S (AGICO Geofysika, Brno), with a sensitivity of 0.5×10^{-8} SI and an accuracy of 0.1 per cent. Each measured sample (standard paleomagnetic specimen of cylindrical size, 2.2 cm height and 2.5 cm diameter) provides a magnetic susceptibility ellipsoid defined by three principal axes $K_1 \geq K_2 \geq K_3$ representing the maximum, intermediate and minimum axes of susceptibility, respectively. In sedimentary rocks magnetic susceptibility K_m originates primarily from three distinct sources: (1) the dominant diamagnetic minerals (quartz or calcite), (2) the paramagnetic minerals (clays and other Fe-bearing silicates) and (3) diluted ferromagnetic minerals (magnetite, hematite and pyrrhotite), depending on their relative proportion (Rochette *et al*. 1992). Generally K_m ranges between low negative values and low positive values (from -10×10^{-6} SI to 10×10^{-6} SI). In Fe-bearing silicate rocks K_m covered susceptibilities up to 500–1000 $\times 10^{-6}$ SI whereas ferromagnetically dominated rocks are generally characterized by values higher than 1000×10^{-6} SI. The lack of paramagnetic minerals tends to decrease the limit of influence of ferromagnetic fraction on magnetic susceptibility.

The magnetic fabric in a rock is typically defined using the orientation of either the magnetic foliation, that is, the plane containing the K_1 and K_2 axes when $K_1 \approx K_2 \gg K_3$, or the magnetic lineation, that is, the direction of the K_1-axis. These two parameters can be defined for a single sample or at the scale of a site corresponding to a collection of about 10 measured specimens. Numerous studies of weakly deformed rocks in fold-and-thrust belts led to a distinction of two fundamental kinds of magnetic fabrics related to tectonic deformation (e.g. Fuller 1964; Kligfield *et al.* 1977; Rathore 1979; Borradaile & Tarling 1981; Kissel *et al.* 1986; Lowrie & Hirt 1987; Aubourg *et al.* 1991; Borradaile 1991; Averbuch *et al.* 1992; Parés *et al.* 1999; Lüneburg *et al.* 1999). The first type is the intermediate fabric characterized by the magnetic lineation still contained within the bedding but clustered at right angle to the shortening direction, whereas the K_3 is leaving the pole to bedding and exhibits a girdle distribution around K_1. This fabric can correspond to an intersection fabric because K_1 generally lies parallel to the intersection between bedding and incipient cleavage (Averbuch *et al*. 1993; Henry 1997) and can result from the sum of two planar and intersecting fabrics (Housen *et al.* 1993; Callot & Guichet 2003). The second type is the tectonic fabric characterized by K_3 parallel to the shortening direction. K_1 is either parallel to the intersection between the bedding and the incipient cleavage or exhibits a girdle around K_3. This fabric, also called the LPS fabric (Graham 1966), supposes coaxial deformation with a shortening direction within the bedding plane. Finally, it is assumed that these fabrics evolved from sedimentary type to tectonic type through an intermediate fabric stage with increasing deformation.

To characterize the magnetic fabric of rocks at Sheep Mountain and its relationship to folding, we sampled 431 cores, from 42 sites in various formations with carbonate and sandstone lithologies of the Sheep Mountain anticline: six sites (71 samples) in the Amsden formation along the hinge line where it crops out preferentially, 12 sites (115 samples) in the Tensleep formation and 14 sites (129 samples) in the Phosphoria formation, rather well distributed on the fold structural surface (Fig. 2). Those sites belong to three structural positions: the forelimb, the backlimb and the hinge. Additionally, 10 sites (116 samples) were sampled in the Mesozoic formations surrounding the anticline. At each site, 7–13 plugs were cored using a gasoline powered portable core-drill.

In order to identify ferromagnetic minerals and to constrain their relative contribution to the magnetic susceptibility and its anisotropy, different rock magnetic measurements were carried out on representative samples. Hysteresis measurements were performed with a in-house constructed magnetometer (M. Legoff, private communication, 2008) and the thermomagnetic curves (K–T) were measured using a spinner kappabridge KLY-3S (AGICO, Brno). We carried out a stepwise demagnetization of three-axes isothermal remanent magnetization following the protocol proposed by Lowrie (1990). With an impulse magnetizer (IM-10), samples were first magnetized along three perpendicular directions with three decreasing successive magnetic fields (1200, 500 and 100 mT); these were next thermally demagnetized stepwise up to 600 °C in step of 50 °C and measured with a JR-6 spinner magnetometer (AGICO, Brno). Depending on the expected Curie temperature we applied finer steps around 120 °C for goethite, 325 °C for pyrrhotite and 580 °C for magnetite.

3.2 Anisotropy of *P*-wave velocity

Previous studies have focused on the seismic or elastic anisotropy of a wide range of rocks (e.g. Birch 1960; Birch 1961; King 1965; Kern *et al.* 1997; Mainprice *et al.* 2000) to get information on microstructures (Louis *et al.* 2003, 2006). For these measurements, six large samples (0.1–0.5 m) were collected from three distinct

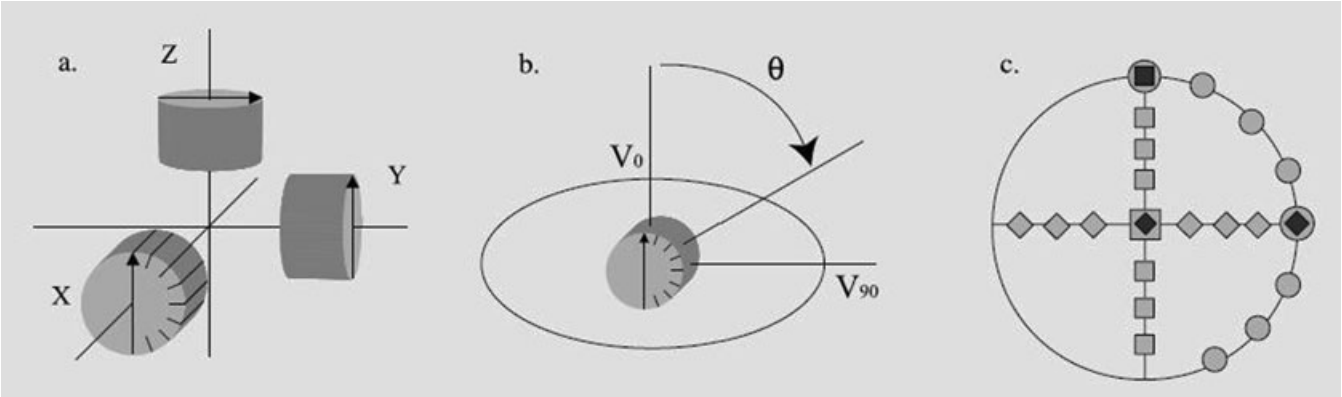

Figure 3. Measurements performed to characterize velocity anisotropy. (a) Respective position of the three oriented core samples with the eight measurement directions indexed on the X sample. (b) Example of a measurement path starting from the *Z*-axis. (c) 24 measured positions in equal-area stereographic projection (after Louis *et al*. 2006)

structural positions (backlimb, forelimb, hinge) and two lithostratigraphic units (three samples from the Phosphoria formation and three samples from the Tensleep formation). We then followed the protocol proposed by Louis *et al*. (2004), in which a triplet of cylindrical standard plugs (diameter of 25 mm and height of 22.5 mm) are drilled along three perpendicular directions from each available block. The orientation reference is based on the normal to the bedding (*Z*-axis), the bedding strike (*X*-axis) and the bedding dip direction (*Y*-axis, Fig. 3a). The ultrasonic measurements were conducted using an ultrasonic pulse generator (Panametrics 5058 PR) with an output voltage up to 900 V, *P*-wave transducers (Accuscan) with a resonance frequency of 0.5 MHz, and a digital oscilloscope (HP54603B) connected to a PC for data acquisition and analysis. For each measurement the piezoelectric transmitter and receiver were located at diametrically opposite positions on the circular cross-section of a sample, and the time of propagation of the ultrasonic wave needed to cross the sample was measured. Measurements are performed every 22.5° (Fig. 3b), so that 24 measurements in total are available for each block. However, only 21 of them are independent since three directions are sampled twice (Fig. 3c). These redundant directions allow to establish a kind of correction or balancing between the measured values in order to correct for the non-reproducibility of the measurements from sample to sample (Louis *et al.* 2004). So, we can virtually consider that all the measurements have been made on a same block. Data were acquired for each sample in a dry state and after saturation with distilled water. Accounting for the errors made when picking the first arrival and measuring the sample diameter, we estimate the standard error for the measurements on nominally dry and saturated samples to be 0.03 and 0.02 km s^{-1}, respectively (Louis *et al.* 2003).

Based on Thomsen's (1986) analysis, generalized by Tsvankin (1997) from a transverse isotropic to an orthorhombic material, Louis *et al*. (2004) concluded that the velocity can be described by a symmetric, second rank tensor V_{ij} so that the *P*-wave velocity for propagation along the direction n_i is given by $V_{ij}n_in_j$. Accordingly, they proposed a methodology whereby the *P*-wave velocities in multiple directions are fitted to the tensor $V = V_{ij}n_in_j$ (Nye 1957), with the directions and magnitudes of the three principal axes corresponding to the eigenvectors and eigenvalues of this symmetric tensor.

At laboratory conditions (no confining pressure) the anisotropic behaviour of rocks with respect to the propagation of *P* waves will be mainly controlled by microstructures (at μm scale) leading to a reduction of the inter- or intragranular cohesion. Such microstructures can be the pore network, the microfractures and the contacts between grains (Louis *et al.* 2005). Considering the simple case of an elliptic pore space, the maximum velocity will be observed in the direction of long axis of the pore. In the case of a planar distribution of cracks or pressure solution cleavage planes, *P*-wave velocity is greatly reduced along the direction normal to the plane. A preferred orientation of intergranular contacts will be characterized by a maximum velocity normal to it. However, one must keep in mind that the resulting acoustic fabric is a composite of these fabrics.

3.3 Fry 2-D strain analysis

The Fry method characterizes 2-D finite strain by measuring centre-to-centre distances between particles in a photomicrograph (Fry 1979). Erslev (1988) modified the method by normalizing the centre-to-centre distances to reduce the influence of 2-D grain size. This new method is called the 'normalized Fry method' (Erslev 1988; Dunne *et al.* 1990). The result is a better-defined strain ellipse. In sandstones, strain within the bedding plane is assumed to be a proxy for layer-parallel tectonic shortening, whereas strain tends to occur perpendicular to bedding for pre-tectonic compaction (Burmeister *et al.* 2009).

For 11 selected plugs of Amsden and Tensleep formations from the Sheep Mountain Anticline, thin sections were cut and oriented within a plane parallel to the bedding. Those thin sections were analysed for 2-D bedding-parallel strain with the normalized Fry method (Erslev 1988; Dunne *et al.* 1990; Burmeister *et al.* 2009). For those analyses, we took photographs of oriented thin sections. We used a computer program to locate at least five points for each grain along the boundaries of 200–300 grains in each digital photomicrograph. Up to five oriented microphotographs (3×2.5 mm^2) were taken to characterize optically the microscopic texture. Images were processed either through bulk extraction of the quartz grains through digital processing of polarized pictures, or by manual extraction of the grain boundaries on normal light pictures. We performed a hot-cathodoluminescence analysis of the Amsden (Fig. 4a) and Tensleep (Fig. 4b) sandstones in order to detect microcracks in quartz grains and to identify optically continuous overgrowth cements that might confuse original grain boundaries and produce errors in locating grain centres (see Dunne *et al.* 1990).

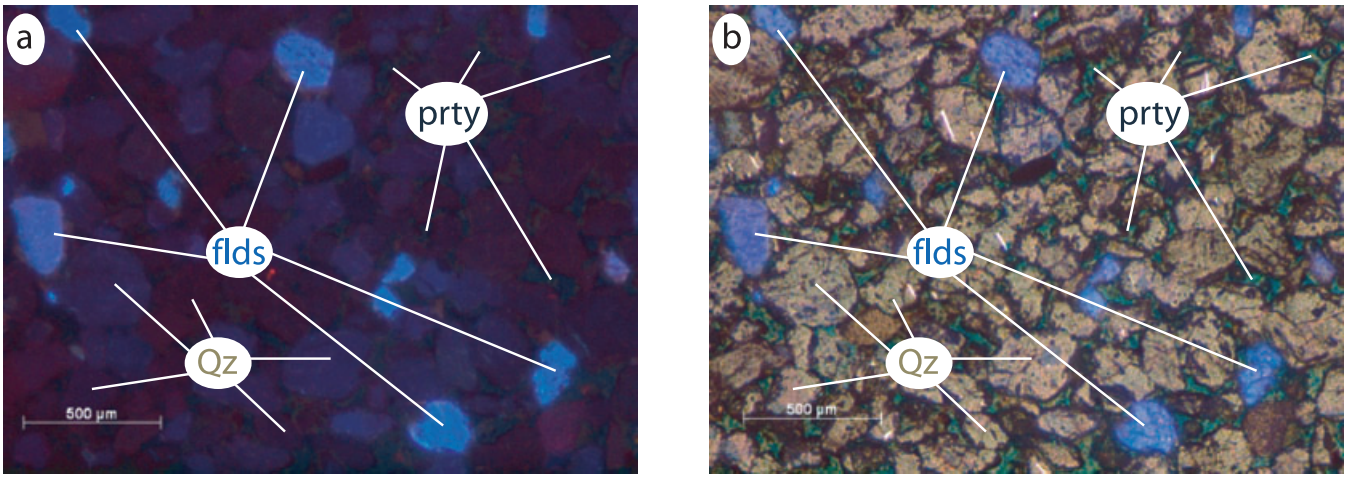

Figure 4. (a) Colour-scanned hot-cathodoluminescence image showing quartz (Qz) and feldspar (flds) grains without continuous overgrowth cements (orange). (b) Same image obtained under natural light. Prty, pyrrhotite.

4 RESULTS

4.1 Bulk magnetic susceptibility and rock magnetism

Bulk magnetic susceptibilities are mostly between -10×10^{-6} and 10×10^{-6} SI, except for a few sites from the Phosphoria formation and the Mesozoic formations (Fig. 5). This range of magnetic susceptibility indicates a diamagnetic contribution to the signal together with a small contribution of paramagnetic phyllosilicates and clays, and/or ferromagnetic minerals. In the vicinity of zero bulk susceptibility, the P parameter increases and its value can exceed 1.5. This strong increase is clearly associated to the near zero susceptibility effect that can be observed in diamagnetic rocks (calcite or quartz rich, Hrouda 1986; Rochette 1987; Borradaile 1988; Hrouda 2004). In the sandstones, samples from the Amsden formation show positive magnetic susceptibilities whereas those from the Tensleep formation are distributed around zero. In carbonates from the Phosphoria formation, the magnetic susceptibilities are mostly diamagnetic with a few sites that show abnormally high values corresponding to an increase in ferromagnetic fraction. Thus, considering that calcite and quartz have intrinsic susceptibilities around -14×10^{-6} SI, the sandstones from the Tensleep and Amsden formations show higher content in paramagnetic and ferromagnetic minerals than the carbonates from the Phosphoria formation. In the Mesozoic formations, a stronger influence of ferromagnetic fraction is observed with susceptibilities higher than 70×10^{-6} SI. Above this limit, P values increase sharply up to values close to 1.25, which can be considered as values above the upper limit of the paramagnetic contribution (Rochette *et al.* 1992).

Three axes IRM thermal demagnetization curves provide evidence for the presence of magnetite with unblocking temperature around 580 °C in almost all heated samples (Fig. 6). Some samples, mainly the carbonates from the Phosphoria formation, show the presence of a high-coercivity phase with unblocking temperature higher than 580 °C (Fig. 6). This phase is assumed to be hematite. In some cases, very small amount of pyrrhotite can be identified with a short drop in magnetization around 380 °C. This pyrrhotite is mostly identified in sand-rich lithologies.

On all investigated samples Curie/Néel temperature (K/T curves on Fig. 6) is observed close to 580 °C supporting that magnetite is the dominant phase. Hopkinson peak, characterized by a sharp enhancement of magnetic susceptibility just preceding (520–580 °C) the Curie/Néel point, is also observed during heating. This peak is attributed to the presence of single domain ferromagnetic grains. However, mineralogical alterations during heating, for instance transformation of low temperature phases into more susceptible phases, can also produce an increase of magnetic susceptibility. This increase is well identified on cooling curves where the susceptibility is systematically much higher than those of the heating curves (Fig. 6). There is no evidence for the presence of hematite in these K–T experiments. The apparent absence of hematite may be due either to its complete break down into magnetite during heating, which requires strong reducing conditions, or to the fact that in a low magnetic field the susceptibility of hematite is negligible with respect to that of magnetite. However, the apparent absence of hematite may be also explained by different experimental conditions, particularly the size of samples (cylindrical specimen of about 10 cm^3 for three-axis IRM, a few mm^3 of powder for K–T curves). The fact that the room temperature magnetic susceptibility measured between each step of thermal demagnetization of the three-axes IRM is not strongly modified by the thermal heating (Fig. 6) is used as evidence for the natural origin of hematite in our samples.

4.2 Magnetic fabrics

The magnetic fabrics measured in this study will be described in terms of their location in the fold: forelimb, hinge and backlimb, and their belonging to a particular lithology: sandstones or carbonates. The effect of near-zero susceptibility observed on the P parameter forbids any use of the tensorial statistics provided by Jelinek (1978). We will therefore present the results in density contour plots of the principal axes (Kamb method provided by stereonet program V.6.3.3). Despite the fact that this approach does not calculate mean magnetic axes normal to each other as provided by tensorial methods, it gives the possibility to extract graphically separate modes in the distribution (Borradaile 2003). Thus, both maximum and minimum axes will be presented separately, and distribution will be evaluated individually. All the AMS data are plotted in untilted position.

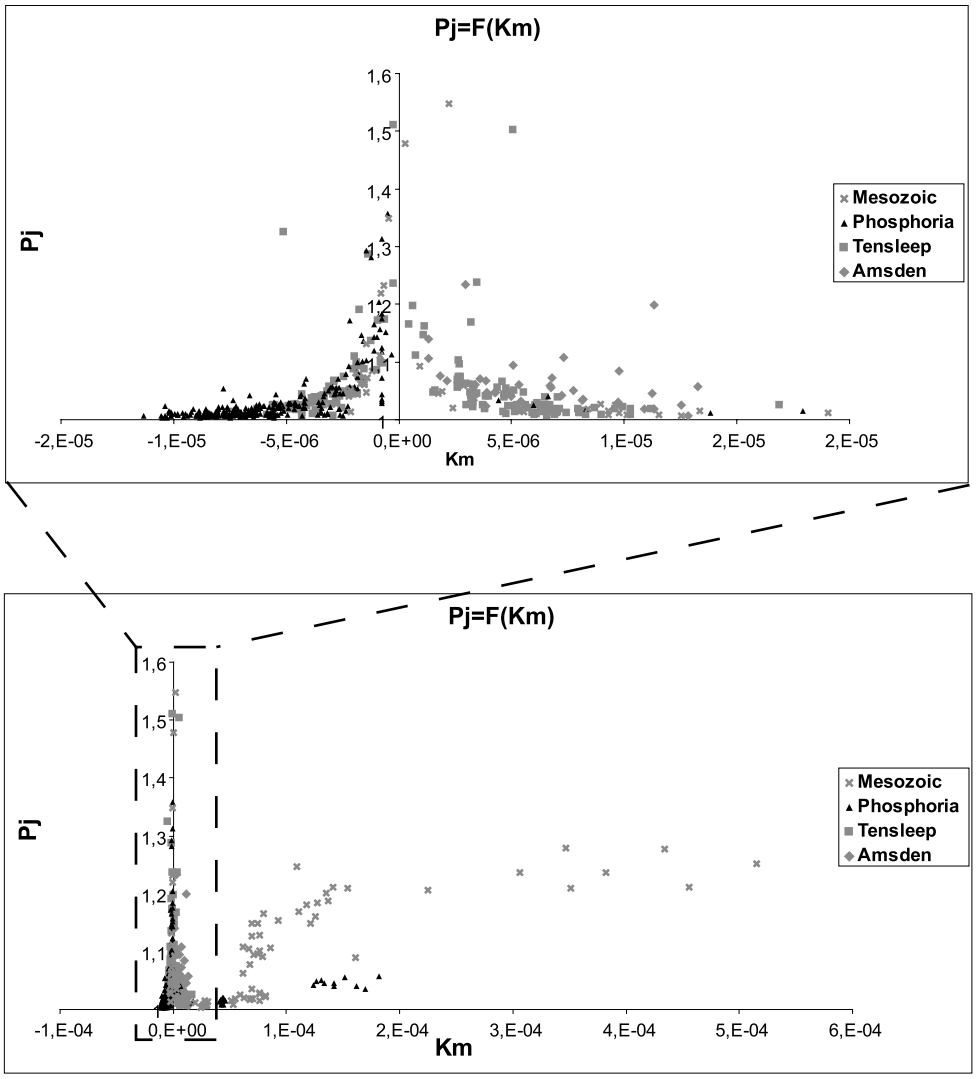

Figure 5. P versus Km diagram for the Sheep Mountain anticline sites. Diamonds, samples from Amsden formation; squares, samples from Tensleep formation; triangles, samples from Phosphoria formation; crosses, samples in Mesozoic formations.

4.2.1 Sandstones

All the investigated sandstones show that orientations of magnetic susceptibility axes are controlled by the plane of bedding (Fig. 7a). In the forelimb, the magnetic fabrics are planar oblate with the maximum axes K_1 scattered in the plane of bedding, the minimum axes K_3 being on average normal to it. These fabrics are confidently interpreted as sedimentary fabrics. A similar fabric is observed in the backlimb but with significantly more clustering of K_1 close to the direction of fold axis (NW–SE) in the plane of bedding. Such a fabric, mixing both the shortening direction and the pole of bedding, can be interpreted as an intersection type fabric of tectonic origin (Henry 1997). This kind of fabric also indicates that sandstones are deformed by pre-folding LPS. In the hinge, the distribution of K_3 is characterized by a girdle in a vertical plane roughly oriented 20°N with two maxima (Fig. 7a). The first maximum is related to the pole of bedding and the second normal to it, in the plane of bedding. Whereas K_1 orientations are scattered in the plane of bedding, a closer inspection reveals a maximum density contour close to 100°N almost perpendicular to the plane of the girdle defined by K_3. Therefore, a linear fabric with a girdle distribution of K_3 characterizes the orientation distribution of K_1 and K_3 in the hinge. This kind of distribution can be interpreted as a competition between intermediate and true tectonic fabrics. The inferred shortening direction, normal to the magnetic lineation and parallel to the K_3 girdle, is oriented 020°N–030°N, which is close to the one defined from the backlimb data.

4.2.2 Carbonates

Because of a poor exposure of carbonates at the hinge, only the forelimb and the backlimb were investigated in the Phosphoria formation (Fig. 7b). In the forelimb, the density plot of the principal magnetic axes shows K_1 scattered in the plane of bedding with a weak maximum close to the fold axis orientation, and K_3 clustered either along the pole of bedding or perpendicular to it. Similarly to sandstones, the magnetic fabric in carbonates from the forelimb can be interpreted as a combination of relict sedimentary fabrics together with intermediate and tectonic fabrics locally. Contrary to all the other fabrics recorded in the fold, the carbonate rocks in the backlimb present a well-defined cluster of K_3, which significantly

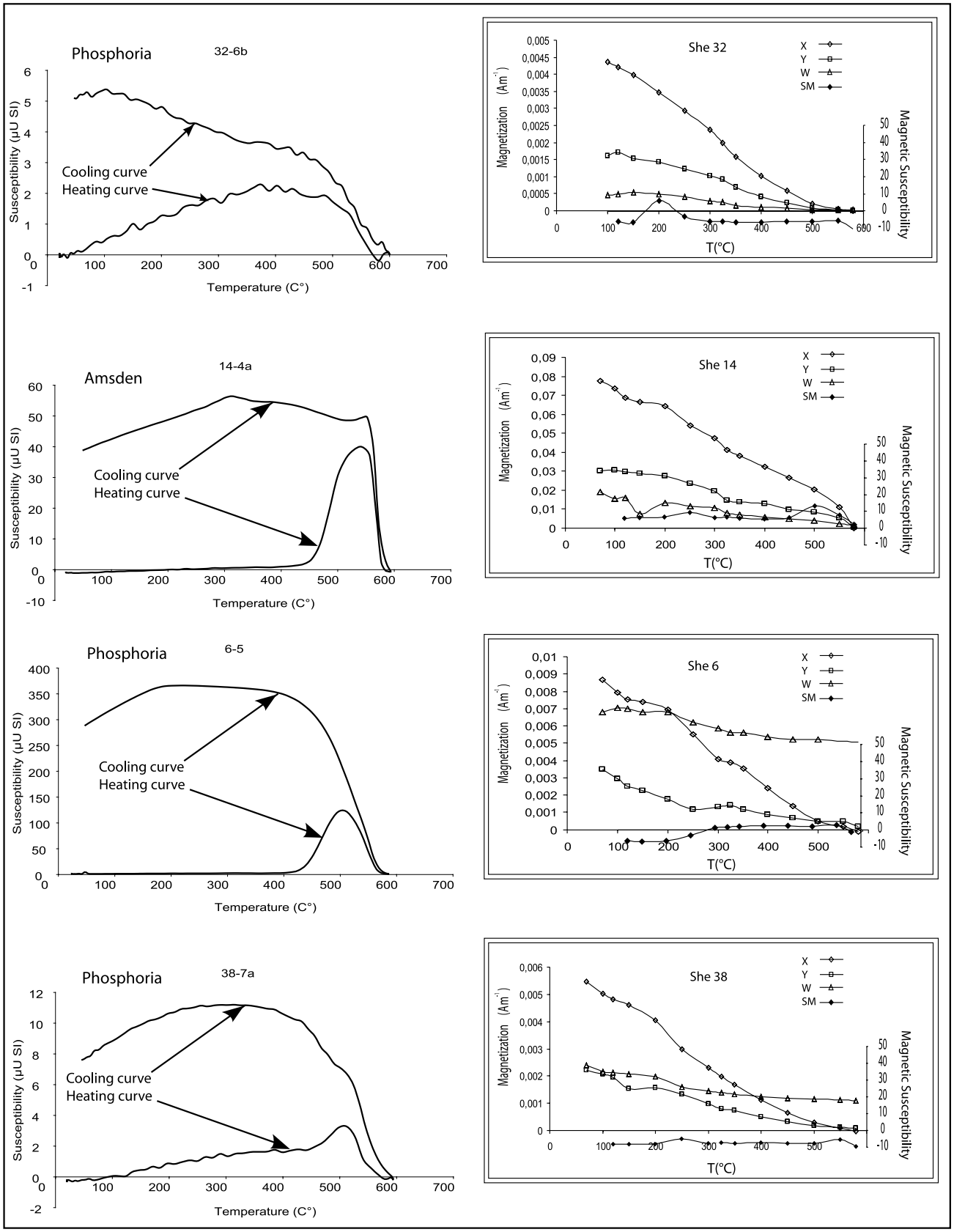

Figure 6. Magnetic mineralogy investigations on representative samples. Left-hand column: examples of reversible (upper) and irreversible (lower) thermomagnetic *K–T* curves indicating the presence of magnetite; Right-hand column: three-axis IRM thermal demagnetization of (Lowrie 1990's method) for four representative samples. SHE 32 and SHE 14 are magnetite-rich sample, SHE6 is a mix of hematite, magnetite and pyrrhotite, SHE 38 is a mix of hematite and magnetite.

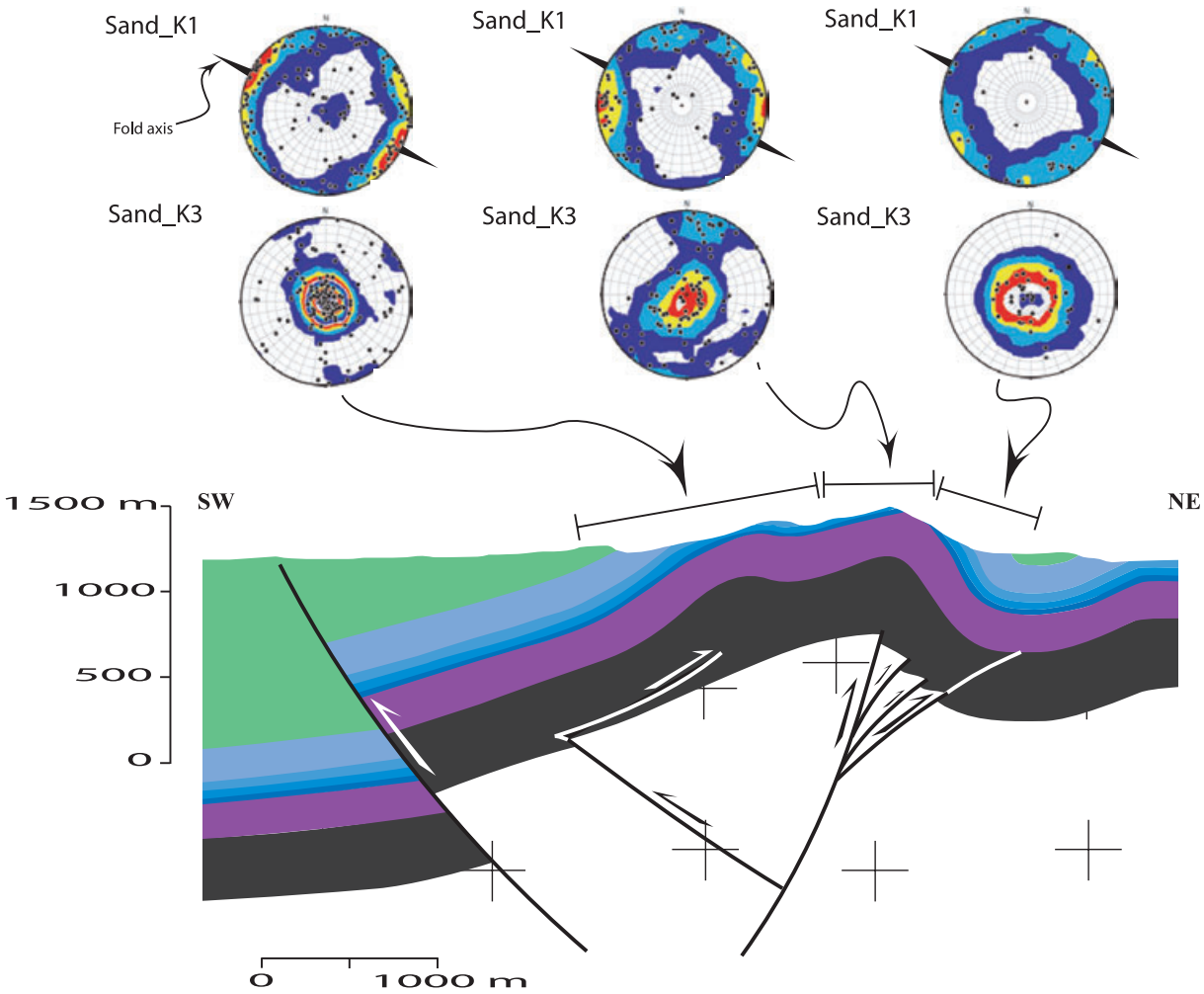

Figure 7. Magnetic susceptibility fabrics as a function of lithology and structural position. The principal susceptibility axes from each site are gathered on lower hemisphere, equal area, stereographic projections of maximum and minimum principal axes [K_1, K_3] from the mean AMS data from Sheep Mountain anticline. The pole density (counted with a spherical Epanechikov kernel colored with an arbitrary scale) is shown and all stereoplots are represented with bedding dip removed. (a) Sand: Sandstone formations. (b) Carb: Carbonate formations. (c) Meso: Mesozoic formations. (for the stratigraphic log see Fig. 1)

deviates from the pole of bedding. K_1 axes lie within a girdle with a higher clustering along the intersection with the bedding plane (Fig. 7b). Similarly to sandstones, this higher clustering of K_1 axes is trending ∼120°N, close to the trend of the fold axis (Fig. 7b). This type of fabric may be associated to the regional shortening direction, but the obliquity of the magnetic foliation with respect to the bedding plane is inconsistent with standard LPS fabrics. By comparison with other fabrics observed in the fold, this is interpreted as bed-parallel shearing, which appears to be more evolved here. It is worth noting that similar oblique fabrics were also encountered in the forelimb of the Tadighoust anticline from South Atlas Front by Saint-Bezar *et al*. (2002).

4.2.3 Mesozoic formations

Mesozoic formations are distributed in the foreland, and at the rear of the Sheep Mountain anticline. In the foreland of the anticline, K_1 is statistically lying within the bedding with a weak concentration parallel to the local fold axis (Fig. 7c). The local rotation of the K_1 axes can be related to the data of sites 30, 33, 34 and 41 which have their K_1 clustered around the local fold axis (Fig. 7c). The distribution of K_3 shows an elliptical shape and is distributed between the pole and the plane of bedding. This fabric is interpreted as a superposition of both relict sedimentary (Sites 28, 29) intermediate (33, 34, 41) and tectonic (30) fabrics. At the rear of the fold, K_1 show scattering in a plane with a concentration parallel to the fold axis. But this plane is oblique to the bedding plane and K_3 is tilted toward the south. This obliquity is characteristic of this part of the fold.

4.2.4 Synthesis

In summary, both in sandstone and carbonate lithologies, we observe intermediate to true tectonic fabrics in the backlimb whereas sedimentary to intermediate fabrics are present in the forelimb. When a tectonic fabric is identified, magnetic lineation is trending close to the fold axis. Unusual tectonic fabrics are observed in the carbonates from the backlimb, with magnetic foliation planes oblique to the bedding, which are related to bedding-parallel shearing during folding. Samples from the Mesozoic formations give quite different orientations of magnetic lineations, in accordance with the local fold orientations in the foreland. At the rear of the fold, the magnetic

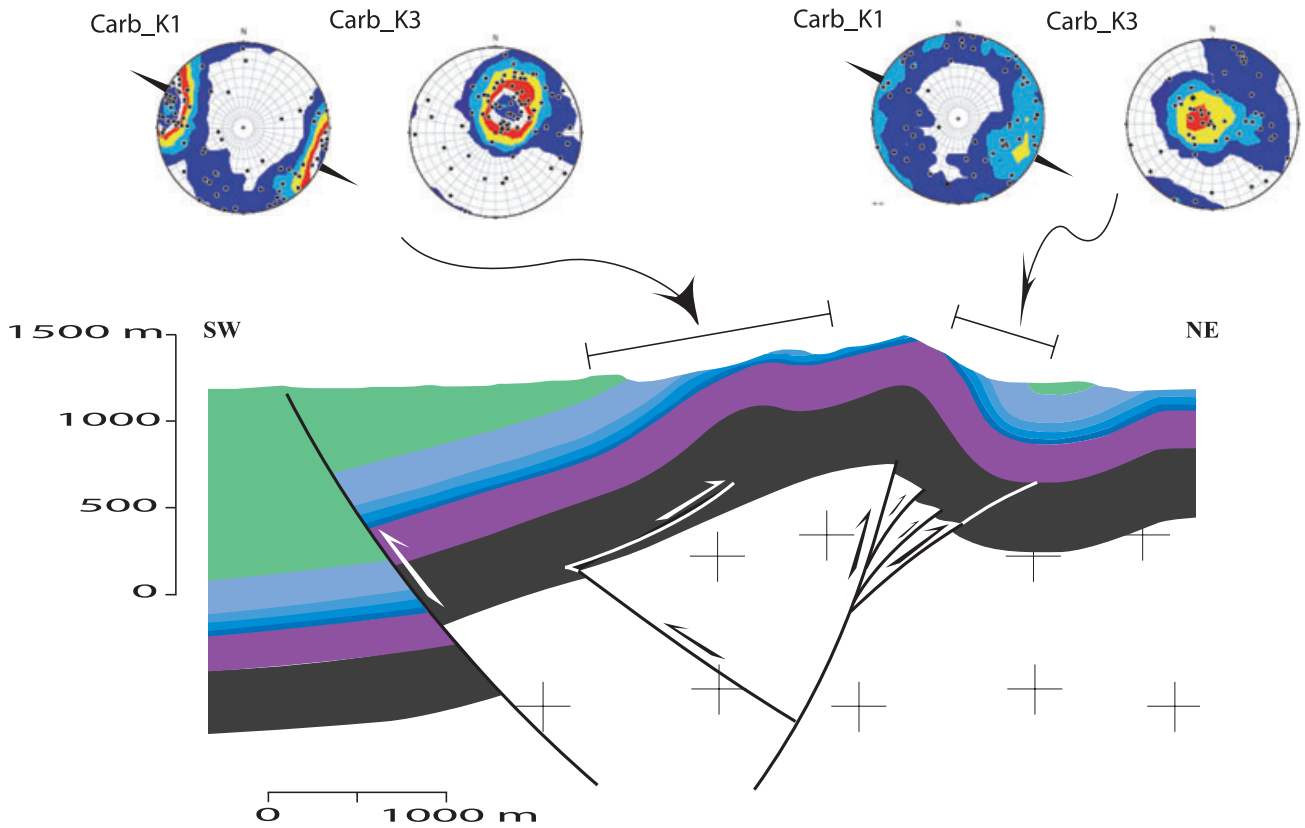

Figure 7. (*Continued.*)

lineation is quite parallel to the fold axis but it is also oblique to the bedding plane. These different results will be discussed in the last section of the paper.

4.3 APWV

Velocity measurements were performed on dry and saturated samples representing carbonate and sandstone lithologies (Table 1). The mean velocity V_m is plotted as a function of porosity (measured by the standard water saturation triple weight method, Rathore *et al.* 1994; Louis *et al.* 2003) on Fig. 8(a). There is an overall tendency for the mean velocity to be higher in the carbonates than in the sandstones, and, within the same lithology, to be lower in high porosity samples. These classical trends are generally explained by the fact that velocities range between the velocities of the mineral grains (intrinsically higher in calcite than in quartz) and those of the mineral–pore fluid filled (air or water) assemblage (Mavko *et al.* 1998).

Despite an overall tendency for the anisotropy to be low (up to 1.17), the P_j versus T plot of Fig. 8(b) indicates that P_j remains nearly unchanged between the dry and the saturated conditions for all the samples apart those from the forelimb of the fold. Concerning the latter ones, one notes a significant variation of P_j, where the anisotropy drops from 1.16 to values lower than 1.03 whereas in the backlimb the decrease is less pronounced and the shape parameter T values are systematically positive and increasingly planar toward the forelimb (Fig. 8). In the hinge, where the anisotropy is the lowest before saturation (around 1.05), the effect of the saturation results in almost no decrease for the carbonate samples or even an increase for the sandstone samples. The significant decrease of anisotropy after water saturation, with a concomitant increase of velocity in the forelimb, is well matched with a model of velocity anisotropy controlled by the porosity and its shape (Kachanov 1992; Louis *et al.* 2003). Following these authors one can consider that a rock made of an anisotropic matrix and an isotropic pore space will be characterized by velocity and anisotropy increase when it is saturated with incompressible material (water). The very strong decrease of anisotropy observed in the forelimb on saturated samples clearly indicates that the matrix is almost isotropic, both in the carbonates and the sandstones. In the backlimb and in the hinge, relatively higher values of the anisotropy after saturation can be explained with a more anisotropic matrix. The special case of the sandstone sample from the hinge, which shows a weak increase of the anisotropy after saturation, indicates that the velocity anisotropy is solely controlled by the matrix anisotropy.

Regarding the directional results and the shape of the ellipsoid, the velocity anisotropy is correlated to the plane of bedding (Fig. 9). Carbonate samples show a planar fabric across the fold. On stereographic projection V_1 and V_2 are located in the plane of bedding with V_1 roughly parallel to the strike of bedding. This distribution is associated with the intermediate type fabric, and can be interpreted as reflecting preferred orientation of pore space with pore long axes horizontal and parallel to the fold axis (Eshelby 1957; Kachanov 1992; Rathore *et al.* 1994). In sandstones, the interpretation of results is less straightforward. The results in the forelimb are in good agreement with the carbonate fabrics described earlier. In the backlimb, although the velocity distribution is always related to the bedding, V_1 is parallel to the dip direction, and V_2 and V_3 are scattered in a vertical plane. In the hinge, V_1 is perpendicular to bedding plane where the V_2 and V_3 are scattered. Keeping in mind that after the saturation the velocity anisotropy is matrix

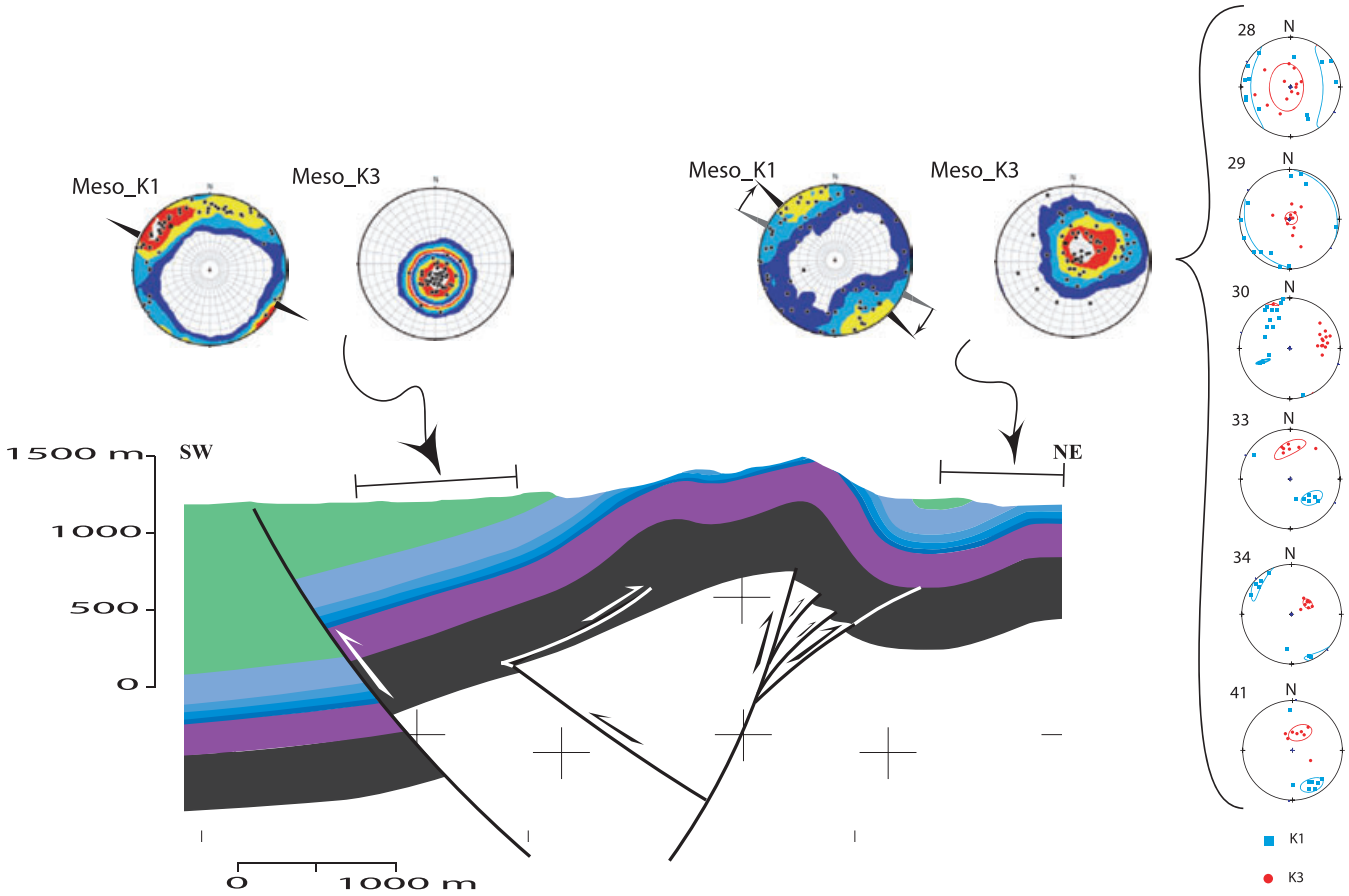

Figure 7. (*Continued.*)

Table 1. Results of anisotropy of *P*-wave velocity analysis.

Samples	*X*	*Y*	Bedding	V_{max} Dec	V_{max} Inc	V_{inter} Dec	V_{inter} Inc	V_{min} Dec	V_{min} Inc	V_{max} (km s^{-1})	V_{inter} (km s^{-1})	V_{min} (km s^{-1})	V_{mean} (km s^{-1})
Dry samples													
SandT BL	44°36,444′ N	108°8,545′ W	105 16 S	196.4	3.3	105.3	18.7	296.2	71.0	4.01	3.84	3.69	3.85
CarbPh BL	44°36,437′ N	108°8,694′ W	120 15 S	167.4	2.8	257.5	1.5	16.4	86.8	6.68	6.51	6	6.40
SandT FL	44°36, 855′ N	108°08,068′ W	135 64 NE	55.8	42.7	323.4	2.6	230.6	47.2	4.6	4.51	4.01	4.37
CarbPh FL	44°36,983′ N	108°07,954′ W	125 62 NE	350.7	21.0	102.2	43.6	242.7	39.0	6.58	6.37	5.71	6.22
SandT H	44°35′364′ N	108°06′255′ W	0 0	111.3	86.3	351.5	1.9	261.4	3.2	2.22	2.14	2.12	2.16
CarbPh H	44°35′394′ N	108°06′198′ W	122 12 NE	123.2	12.8	30.8	10.4	262.8	73.4	5.81	5.69	5.51	5.67
Saturated samples													
SandT BL	44°36,444′ N	108°8,545′ W	105 16 S	190.4	11.1	83.9	55.4	287.5	32.3	4.19	4.02	3.96	4.06
CarbPh BL	44°36,437′ N	108°8,694′ W	120 15 S	315.9	4.5	225.2	9.3	71.4	79.6	6.71	6.59	6.13	6.48
SandT FL	44°36, 855′ N	108°08,068′ W	135 64 NE	331.9	5.3	70.1	57.0	238.5	32.5	5.67	5.63	5.41	5.57
CarbPh FL	44°36,983′ N	108°07,954′ W	125 62 NE	335.0	22.5	122.6	63.9	239.7	12.6	7.13	7.04	6.91	7.03
SandT H	44°35′364′ N	108°06′255′ W	0 0	134.0	62.9	42.7	0.7	312.3	27.1	2.94	2.76	2.7	2.80
CarbPh H	44°35′394′ N	108°06′198′ W	122 12 NE	103.7	9.7	13.7	0.3	281.8	80.3	5.57	5.44	5.36	5.46

supported, we can infer from velocity directions that there is a preferred orientation of the grains related to both shortening direction and bedding.

4.4 Fry strain analysis results

Fry analysis indicates that the Tensleep and Amsden sandstones accumulated only small bedding-parallel shortening strains (Paterson and Yu 1994; Wetmore 2003). Ellipse axial ratios range from 1.059 up to 1.078 for Amsden formation with a mean of 1.07, and range from 1.068 up to 1.146 for Tensleep formation with a mean of 1.105 (Figs 10a and b). The orientations of the long axes of the Fry ellipse are parallel to the direction of the fold axis in the forelimb, hinge and backlimb (Figs 10a and b, and Table 2). This is also highlighted by the comparison with the density contours of the AMS K_1 axes distribution for the sites investigated by the Fry method (Fig. 10c). One can note a difference between these two directions, which can be explained by the fact that the long axes of the Fry ellipse reflect

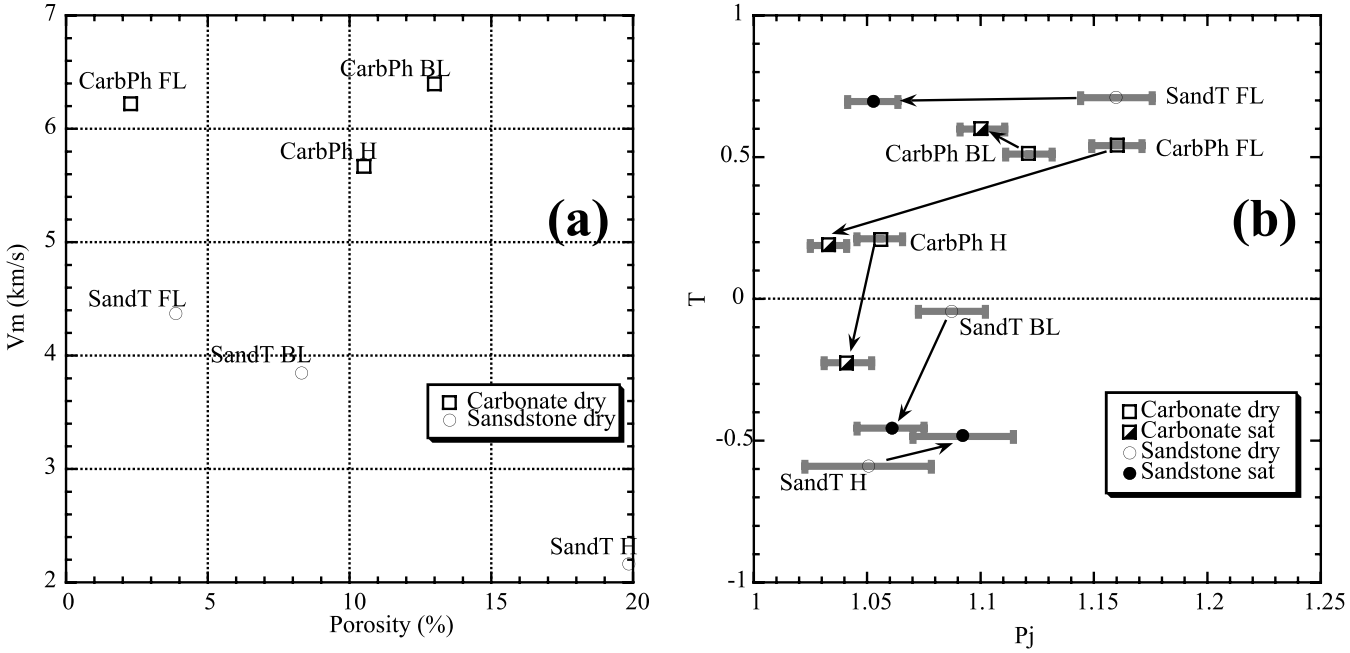

Figure 8. (a) Variation in mean velocity distribution V_m versus porosity (measured by the standard water saturation triple weight method) and (b) Evolution of mean anisotropy parameters P_j versus T in the Tensleep formation (SandT) and Phosphoria formation (CarbPh) from the forelimb (FL), the hinge (H) and the backlimb (BL). T is the shape parameter and P_j the Jelinek anisotropy parameter (Jelinek 1981).

the preferred grain shape whereas AMS K_1 axes record the shape of the coatings that fill the remaining porosity between the grains (Fig. 11).

In the samples from the Amsden and the Tensleep formations, the clay- and silt-rich matrix constitutes 5–20 per cent of the rock volume (Fig. 11). Hot-cathodoluminescence microscopy (Fig. 4) reveals the absence of microcracks with the presence of quartz grains with sutured and interpenetrated boundaries (Fig. 11).

5 DISCUSSION

In fold-and-thrust belts, AMS studies have been proven to be successful in showing that during the LPS stage, AMS fabrics evolve from sedimentary fabrics to intermediate and true tectonic fabrics (e.g. Averbuch *et al.* 1992). The fabrics characterized in Sheep Mountain Anticline are coaxial both with (1) the plane of bedding (i.e. magnetic foliation is either parallel or normal to the bedding, and magnetic lineation parallel to the fold axis) and (2) the deformation axes, indicating that they were acquired during an early stage of deformation when the bedding was horizontal. This pattern of deformation has been already observed mostly in sandstones, shales and silts and in few limestone lithologies (Aubourg *et al.* 1997; Sagnotti *et al.* 1998; Pares *et al.* 1999; Saint-Bezar *et al.* 2002; Evans *et al.* 2003; Robion *et al.* 2007). During folding, the imposed shear direction in the different parts of a fold can be also recorded by the AMS fabric, depending on the kinematic of folding (fault-bend fold, fault-propagation fold, Trishear fold, etc., Frizon de Lamotte *et al.* 2002). This was particularly well demonstrated by Saint-Bezar *et al*. (2002) who reported oblique *syn*-folding magnetic fabrics recorded in the fold forelimb in agreement with the bed-parallel simple shear expected from the kinematics of this type of fold (see Souque *et al.* 2003, for an illustration of kinematics of folding inferred from the magnetic fabric). Concerning the samples from Mesozoic formations in the backlimb, the explanation for the obliquity of magnetic foliation should be linked to sedimentary processes. Oblique magnetic foliation with respect to bedding has been documented in flysch-type sedimentary deposits by Hrouda & Jezek (1999) and Aubourg *et al*. (2004).

However, at Sheep Mountain Anticline, the spatial distribution of the magnetic fabrics deviates from this general model. The differences are twofold: (1) there is no clear LPS magnetic fabric recorded in the forelimb, and (2) *syn*-folding fabrics, oblique to the bedding, are only recorded in the backlimb in the carbonate formations. These results question the origin and nature of the rock fabrics and should be compared to other independent microscopic and mesoscopic stress–strain indicators (see Bellahsen *et al.* 2006a; Amrouch *et al.* 2010).

5.1 Reliability of ASM measurements and origin of ASM fabrics in low-susceptibilty rocks

It is often claimed that the measured magnetic anisotropy in low-susceptibility (diamagnetic) rocks such as carbonates or sandstones is difficult to interpret and can be locally controlled by very few para- and ferromagnetic grains (Borradaile & Gauthier 2003). This is particularly true for the degree of anisotropy that increases dramatically for samples with small mean susceptibility as shown in Fig. 5. One might also ask whether the directions of anisotropy are biased for samples with mean susceptibilities close to zero. Our study shows that: (1) when the magnetic directions are clustered, they are systematically related to the regional structures. This is observed in the backlimb where the peak densities of K_1 are parallel to the fold axis (Fig. 7); (2) there is a good agreement of the structural directions (i.e. fold axis) inferred from the two lithologies especially in the backlimb. (3) Both the carbonates and the sandstones show evidence that pressure solution processes were active during deformation (Fig. 11). This partially helps to overcome problems related to the magnetic mineralogy, because the magnetic anisotropy measured in sandstones is not due to quartz, which is intrinsically isotropic, but due to a very small amount of

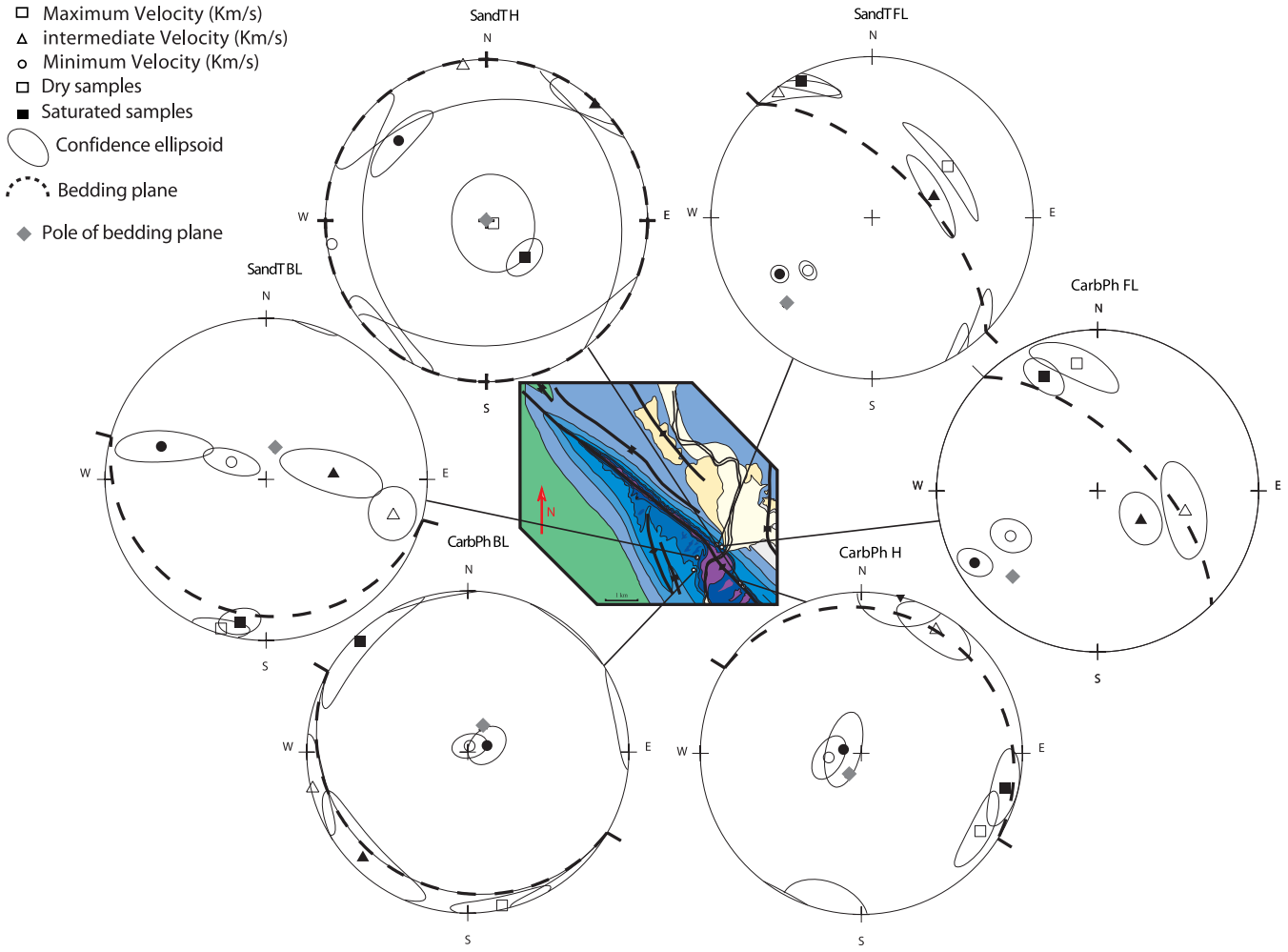

Figure 9. APWV measurements over the Sheep Mountain anticline for dry (white symbols) and saturated (black symbols) conditions. Equal area, lower-hemisphere stereoplots, with mean bedding plane shown as a great circle with its pole as grey diamond. Squares correspond to the maximum velocity axes (V_1), triangles to the intermediate velocity axes (V_2), and circles to the minimum velocity axes (V_3). CarbPh, Phosphoria formation; SandT,Tensleep formation; FL, Forelimb; H, Hinge and BL, Backlimb.

phyllosilicates and/or oxides (Evans *et al.* 2003), whereas in carbonates (more than 99 per cent by volume) it is due primarily to the calcite which is highly anisotropic ($P_j = 1.1$, Owens & Bamford 1976; Schmidt *et al.* 2006). This last point is important as it suggests that the measurement of magnetic susceptibility is reliable in carbonates, since it corresponds to the contribution of several hundred thousands of grains per sample. Moreover, as phyllosilicates or oxides minerals (which are significantly anisotropic) control the anisotropy in the sandstones, identifying similar magnetic lineations in both lithologies is an additional argument in favor of a tectonic origin for the magnetic fabric (Fig. 11a). Thus, it is concluded that the magnetic fabrics measured are weakly organized in the sandstones because there is a very small contribution of paramagnetic and oxides to the signal whereas in the carbonates this is due to a slight preferred orientation of the calcite grains and the intersection between the bedding and the pressure-solution cleavage planes.

5.2 Interpretation of the velocity measurements, and integration of the data set

The investigation of the effect of water saturation on APWV clarifies the various sources of anisotropy depending on the location within the fold. Note that these variations are more controlled by the structural position than by the lithology of the samples (Fig. 8). Two outcomes on anisotropy are observed after water saturation: (1) in the samples from the forelimb, we observe a significant decrease of the anisotropy (drop from 2.5 to 0.5 per cent) whereas (2) we note a relatively less significant decrease or even an increase in the backlimb and hinge. The extreme case is obtained for sandstones from the hinge, whose anisotropies increase after saturation (Fig. 7). The forelimb behaviour can be easily captured with a simple effective medium model in which an anisotropic pore space with low aspect ratio is embedded into an isotropic matrix (Kachanov 1993; Louis *et al*. 2003). In this case, only the anisotropy of pores contributes to the anisotropy of seismic velocities, and adding water hides the effect of porosity. The response of carbonate samples from the backlimb and the hinge, which show a less reduced anisotropy, is probably controlled jointly by an anisotropic porosity and the matrix structure. To explain the increase of anisotropy associated with maximum velocity normal to bedding (SandT H, Fig. 8b), Louis *et al*. (2003) used a spherical grain packing model partly cemented at the grain contact (Dvorkin and Nur 1996). The cement has to be elastic with contrasting properties compared to those of the grains. Increasing the amount of cement between grains will increase the surface of the contact between grains, resulting in the increase of the stiffness of the whole assemblage and of the velocity normal

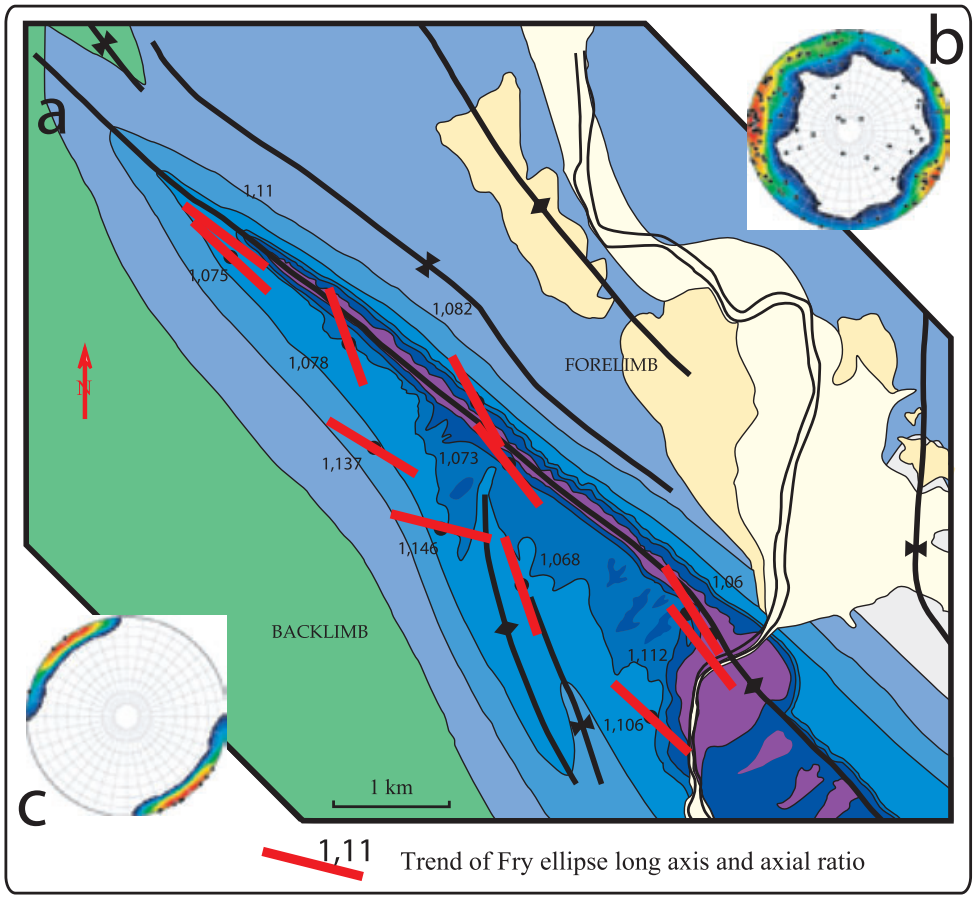

Figure 10. Strain axes deduced from Fry method at Sheep Mountain anticline: (a) Geological map of Sheep Mountain Anticline with long-axis trends and axial ratios of individual bedding-parallel Fry ellipses at sampling locations throughout the study area and (b) trends of all the K_1 axes of AMS fabrics measured from the same samples used for Fry analysis. (c) The lower-hemisphere stereoplot illustrates the long axes of bedding parallel Fry ellipses in the study area (for the stratigraphic log see Fig. 1).

Table 2. Results of Fry strain analysis.

Samples	*X*	*Y*	Bedding	Formation	Position	Trend of Fry ellipse long axis	Axial ratio
1	44°36,915	108°8,354	0 0	Amsden	Hinge	147.9	1.060
2	44°36,869	108°8,418	120 13S	Tensleep	Hinge	322.0	1.112
5	44°36,453	108°8,629	120 12S	Tensleep	Backlimb	132.6	1.106
7	44°38,1	108°10,347	118 12S	Amsden	Hinge	160.3	1.078
9	44°37,607	108°9,457	136 9W	Amsden	Hinge	146.4	1.073
10	44°37,046	108°9,465	107 26S	Tensleep	Backlimb	161.2	1.068
12	44°37,826	108°10,348	125 28S	Tensleep	Backlimb	121.3	1.137
21	44°38,522	108°11,065	124 28S	Amsden	Backlimb	312.9	1.075
22	44°38,699	108°11,412	145 19W	Tensleep	Backlimb	127.1	1.110
31	44°30,033	108°9,882	116 78N	Tensleep	Forelimb	151.6	1.082
37	44°37,228	108°10,041	145 39W	Tensleep	Backlimb	284.1	1.146

to the contact. Louis *et al*. (2003) took advantage of this model to infer that, if the distribution of the contacts length increases along one direction (in the bedding plane in case of preferred orientation of grains), one should observe an increase of the velocity normal to it with maximum velocities parallel to the pole of bedding. The anisotropy of the matrix is sufficient to control the velocities, despite the existing anisotropic porosity (SandT H, Fig. 9). This model can explain the velocity distribution in the sandstones from the hinge (Fig. 9). The general interpretation of the APWV results is consistent with the magnetic fabric results in sandstones, with the presence of phyllosilicates and oxides around the quartz grains (Fig. 11a), because of the relationship between the porosity shape and the coating shape. Measurements of APWV for saturated samples in the backlimb suggest that the contribution of the matrix to the signal is higher than in the forelimb.

Integrating the various sources of the anisotropy of physical properties provides new insights into the distribution of deformation within Sheep Mountain anticline. On one hand, we find that the

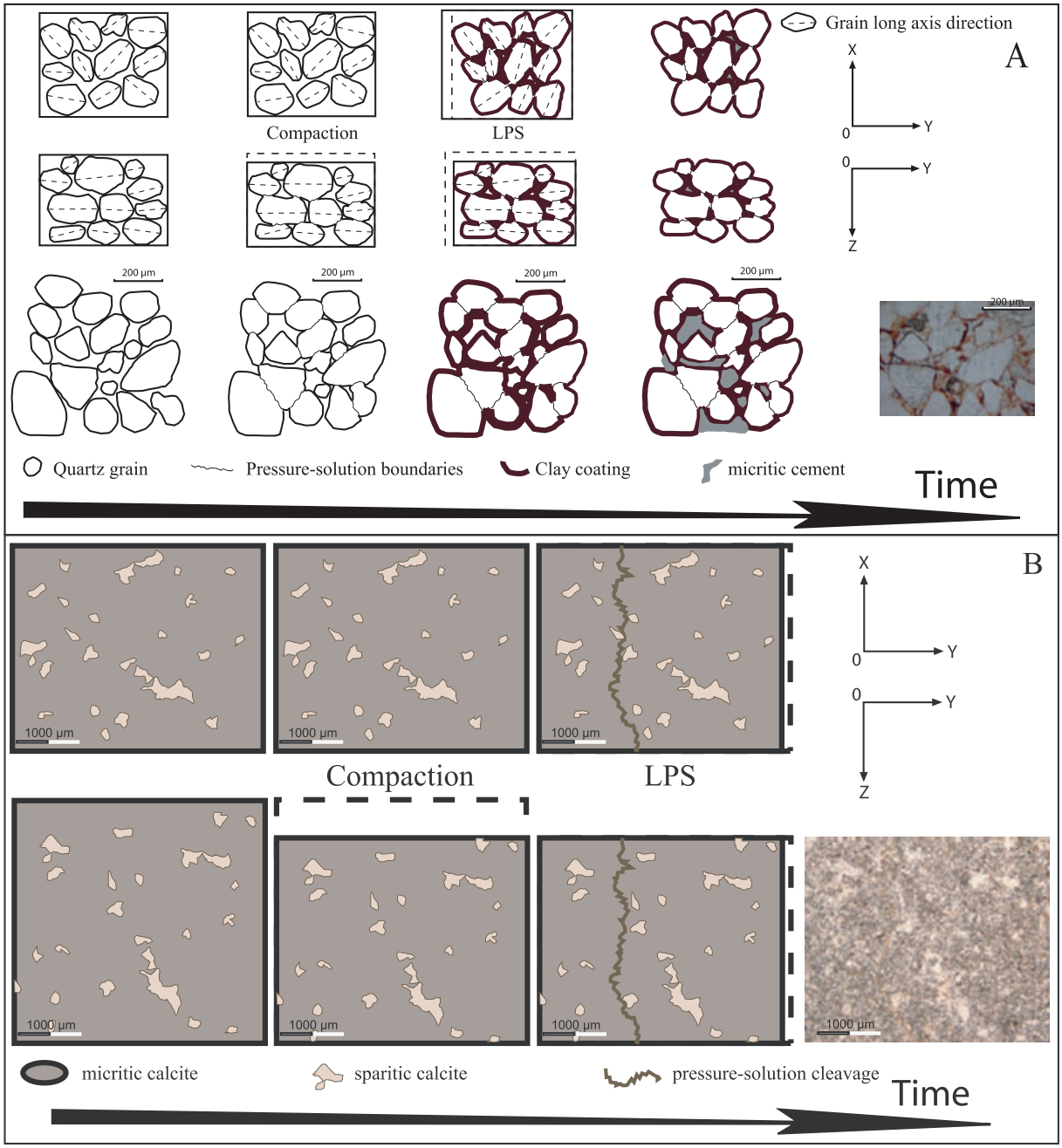

Figure 11. Sketches of different stages of formation/deformation of a sedimentary rock until a final state illustrated by the microphotographs of polished thin sections observed in natural light. (a) Sandstones (Amsden); (b) Carbonates (Phosphoria). *XY* plane is the bedding plane (*X*: Strike; *Y*: dip), *YZ* is the plane perpendicular to the bedding plane.

sedimentary magnetic fabrics were preserved in the forelimb. On the contours diagrams (Fig. 7), we can see that the distribution of the magnetic axes orientation is not very pronounced, suggesting that the anisotropy of the rock is weak relatively to other parts of the fold. This result is in good agreement with measurements of APWV, which indicate that the anisotropy is dominated by an anisotropic pore network embedded into an almost isotropic matrix. In contrast, in the backlimb, AMS records true tectonic strain at the matrix scale. In the sandstones, the magnetic fabrics can be linked to the pre-folding LPS, whereas in carbonates the magnetic fabrics are interpreted to record bedding-parallel shear. Likewise, APWV fabrics in the backlimb are grain-supported, showing that the matrix is more anisotropic in the backlimb than in the forelimb. The direction of anisotropy is roughly related to the plane of bedding indicating that APWV fabrics could also be linked to early stage LPS deformation. It is worth noting that deformation in the front of the fold is preferentially revealed by the porosity, which is systematically oriented with its long axis parallel to the fold axis. The results of the combination of these various approaches allow us to characterize the succession of microscopic deformation mechanisms active before and during

folding of sedimentary rocks (i.e. compaction, pressure-solution) (Fig. 11).

5.3 Comparison with stress–strain tensors derived 7 from calcite twins

Amrouch *et al*. (2010) have investigated the scenario of stress–strain evolution recorded in the folded rocks of Sheep Mountain anticline by combining two techniques for analysing calcite twins. The Calcite Stress Inversion Technique (e.g. Etchecopar 1984; Laurent 1984; Lacombe 2001; Lacombe 2007) allows simultaneous calculation of principal stress orientations and differential stress magnitudes from a set of twin data, therefore allowing to relate differential stress magnitudes to a given stress orientation and regime (e.g. Lacombe *et al.* 2007; Lacombe *et al.* 2009). The Calcite Strain Gauge Technique (Groshong 1972; Groshong 1974) allows computation of the strain ellipsoid. Rock matrix, pre-folding veins and fold-related veins were sampled.

Calcite twin analysis reveals three main tectonic stages (Amrouch *et al.* 2010): two stages of LPS (a pre-folding compression nearly parallel to the fold axis and a pre-folding compression perpendicular to the fold axis), and a stage of post-folding compression also trending normal to fold axis. The first LPS stage likely corresponds to a NW–SE-directed (Sevier ?) compression/shortening. It is observed in both limbs. This LPS is preserved by calcite twinning in the matrix of the Madison and Phosphoria formations. Finite strain and differential stresses related to this tectonic phase remained relatively low (Amrouch *et al.* 2010), in agreement with the absence of signature of this event in AMS, APWV and Fry strain analysis records.

The second LPS stage corresponds to a NE–SW direction of compression/shortening that trends perpendicular to the fold axis. The related stress–strain tensors were obtained from veins from the Madison, Phosphoria and Tensleep formations within both fold limbs. Most samples recorded a dominantly compressional regime. A post-folding stage is also preserved by twin calcite in the veins and matrix from sandstones of the Tensleep formation and from carbonates of the Madison and Phosphoria formations, whatever the orientations of the veins from which measurements were taken. In all tensors the regime is strike-slip in type and the $\varepsilon_{min}/\sigma_1$ axis strikes perpendicular to the fold axis. The results obtained with the two techniques show a very good consistency in terms of orientations of shortening (ε_{min}) and compression (σ_1) and regime for the two LPS stages and the late stage fold tightening, therefore supporting that internal strain of folded strata remained mainly coaxial. Fig. 12 summarizes those results and shows that they are consistent with the results of AMS, APWV and Fry strain analysis. In term of trends, the principal axes of the various tensors have close relationships with the fold structure. We especially point out a good agreement between AMS K_1-axis, APWV V_1-axis and the long-axis of Fry ellipses which strike parallel to the fold axis, and the calcite strain shortening axis, ε_{min}, and the maximum principal stress axis, σ_1, trending perpendicular to the fold axis. On a more quantitative point of view, the information brought by calcite twinning studies and by AMS and APWV studies on the structural history of the fold are complementary. In the pre-folding stage, (σ_1–σ_3) differential stress values were high in the forelimb, about ∼60 MPa (Amrouch *et al.* 2010) whereas internal deformation of the strata there is weak as revealed by AMS (Fig. 12); in contrast, (σ_1–σ_3) differential stress values remain low in the backlimb (∼20 MPa), whereas AMS points

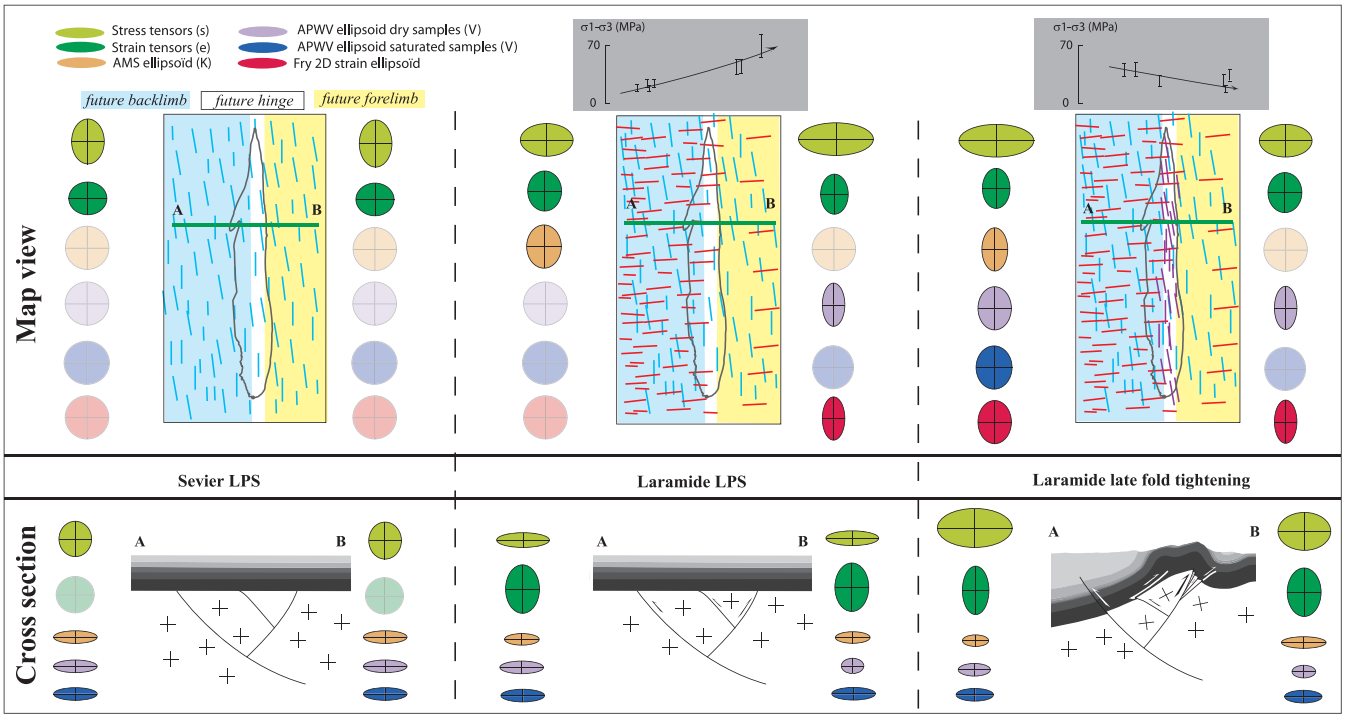

Figure 12. Sketches (sections and map views) of the successive stages of Sheep Mountain anticline evolution, with related AMS and APWV ellipsoids, 2-D Fry strain ellipsoids and stress–strain ellipsoids from calcite twins (Amrouch *et al.* 2010), as well as with distribution and orientation of related fracture sets (Bellahsen *et al.* 2006a; Amrouch *et al.* 2010). In grey rectangles the evolution of differential stresses values through space (backlimb and forelimb) and time (Laramide LPS and Laramide late fold tightening). For the stratigraphic log, see Fig. 1. The dotted line shows the outline of the present-day fold (limits of the outcropping Phosphoria formation) for each step of the scenario. Set I: 110–130°N in blue dash. Set II: 45°N in red dash. Set III: in purple dash. Planar isotropy as transparent circles.

toward significant internal deformation. On the other hand, the post-folding differential stresses were higher in the backlimb (∼40 MPa) than in the forelimb (∼20 MPa), whereas AMS and APWV studies reveal more evolved fabrics in the backlimb than in the forelimb (Figs 7a,b; 8 and 9).

5.4 From the microscopic scale to the fold scale: bridging the gap

The comparison of the anisotropy of rock physical properties across SMA with the differential stress values derived from calcite twins and with the distribution of the different fracture sets outlines the large asymmetry between the forelimb and the backlimb of the fold. This asymmetry is likely related to the way the fold developed above the underlying basement thrust fault (Fig. 1b). The increase in pre-folding differential stresses from the backlimb toward the forelimb is thus related to the stress perturbation induced in the cover by the tip of this underlying thrust fault as earlier suggested by Bellahsen *et al*. (2006b) and Amrouch *et al*. (2010). This stress perturbation prevented, at least partly, the development of Laramide LPS-related set II fractures in the forelimb (see Section 2; Bellahsen *et al.* 2006b); in turn, the limited development of these fractures, together with the weak internal deformation of strata as recorded by AMS and APWV, did not allow stress relaxation during LPS, enhancing stress increase in the forelimb (Fig. 12). Conversely, in most of the backlimb, the underlying fault did not cause any stress perturbation and in addition, stress relaxation occurred by widespread development of set II fractures (Fig. 12) and also by internal strata deformation as recorded by AMS (Figs 7a,b and 12). This explains that in the pre-folding stage, maximum differential stresses recorded by calcite twins in the backlimb are much lower than in the forelimb (Fig. 12). During the post-folding stage differential stress values in the forelimb dropped significantly whereas internal deformation of strata remained limited as suggested by poorly evolved ASM fabrics (Fig. 7) and low anisotropy of the matrix revealed by APWV (Fig. 8). This means that strata of the forelimb were likely simply tilted during folding and did not undergo additional significant internal deformation, late stage fold tightening being mainly accommodated there by newly formed microfaults and compressional reactivation of previously formed set I fracture sets that relaxed stresses (Bellahsen *et al.* 2006a; Amrouch *et al.* 2010). In contrast, strata of the backlimb sustained most of late stage fold tightening without developing much fractures, leading to an increase of differential stresses and development of more evolved ASM fabrics compared to the forelimb.

6 CONCLUSIONS

We carried out a combined analysis of AMS, Anisotropy of *P*-wave velocity and Fry strain in the sandstone and carbonate folded strata of Sheep Mountain Anticline. The results demonstrate a very good agreement between the principal axes of the anisotropy of physical properties of rocks (AMS, APWV), Fry strain axes and principal stress–strain axes derived from calcite twinning (Fig. 12). It further shows a high consistency of the strain ellipsoid orientation with macroscopic fracturing and with the overall anticline geometry (Fig. 12). The other main result of this study is that the structural contrast between the forelimb and the backlimb of the anticline, shown by differential stress values and macroscopic distribution of fractures (Fig. 12, Amrouch *et al.* 2010), is also revealed by the petrophysical characteristics of cored samples (AMS: Figs 7a and b; APWV fabrics, Figs 8 and 9). The analyses of the anisotropy of physical properties of sedimentary rocks, of Fry strain, of calcite twins and of fracture data combined with petrographic and diagenetic observations can therefore be reliably used to unravel the strain history of strata during folding, and to characterize the deformation mechanisms active at various scales during fold evolution.

This study emphasizes the complementary nature of deformation mechanisms active at different scales in accommodating internal strain of folded strata during the different stages of fold development. Especially, micromechanisms appear to be more efficient before and at the onset of folding (LPS) and during late stage fold tightening stages, that is, when the fold itself is not yet and no longer forming, whereas macromechanisms (development of extensional fractures at the hinge or bedding-parallel slip) seem to prevail during folding *ss*.

Finally, the macroscopic asymmetry of the NE-verging SMA, likely related to underlying basement thrust, is also clearly marked at the mesoscopic and the microscopic scales. Structural observations made at the microscopic scale in part of a fold may therefore be relevant to the fold scale.

ACKNOWLEDGMENTS

The author would like to thank Maxime LeGoff and Bernard Henry (St Maur Laboratory, IPGP) for giving access to the paleomagnetic facilities. This paper benefited from discussions with L. Louis, C. Aubourg, R. Swennen and T. Engelder, and from thorough reviews by Ben van der Pluijm and Bjarne Almqvist. J-M Mengus and B. Vincent are thanked for their participation to fieldtrips.

REFERENCES

Amrouch, K., Lacombe, O., Bellahsen, N., Daniel, J.M. & Callot, J.P., 2010. Stress/strain patterns, kinematics and deformation mechanisms in a basement-cored anticline: Sheep Mountain anticline (Wyoming, USA). *Tectonics,* **29,** TC1005, doi:10.1029/2009TC002525.

Aubourg, C., Rochette, P. & Vialon, P., 1991. Subtle stretching lineation revealed by magnetic fabric of Callovian-Oxfordian black shales (French Alpes), *Tectonophysics,* **185,** 211–223.

Aubourg, C., Frizon de Lamotte, D., Poisson, A. & Mercier, E., 1997. Magnetic fabrics and oblique ramp-related folding: a case study from the western Taurus (Turkey), *J. Struct. Geol.,* **19,** 1111–1120.

Aubourg, C., *et al*. 2004. Post-Miocene shortening pictured by magnetic fabric across the Zagros-Makran syntaxis (Iran), in Orogenic Curvature: Integrating Paleomagnetic and Structural Analysises, Geological Society of America Special Paper **383,** pp. 17–40, eds Sussman, A. J. and Weil, A. B., Geological Society of America, Boulder, Colorado.

Averbuch, O. Frizon de Lamotte, D. & Kissel, C., 1992. Magnetic fabric as a structural indicator of the deformation path within a fold-thrust structure: a test case from the Corbières (NE Pyrenees, France), *J. Struct. Geol.,* **14**(4), 461–474.

Averbuch, O., Frizon de Lamotte, D. & Kissel, C., 1993. Strain distribution above a lateral culmination: an analysis using microfaults and magnetic fabric measurements in the Corbières thrust belt (NE Pyrenees, France), *Annales Tectonicae* **VII**(1), 3–21.

Bellahsen, N., Fiore, P. & Pollard, D.D., 2006a. The role of fractures in the structural interpretation of Sheep Mountain Anticline, Wyoming, *J. Struct. Geol.,* **28**(5), 850–867.

Bellahsen, N., Fiore, P. & Pollard, D.D., 2006b. From spatial variation of fracture patterns to fold kinematics: A geomechanical approach, *Geophys. Res. Lett.,* **33,** L02301, doi:10.1029/2005GL024189.

Birch, F., 1960. The velocity of compressional waves in rocks to 10 kilobars. Part I, *J. geophys. Res.* **65,** 1083–1102.

Birch, F., 1961. The velocity of compressional waves in rocks to 10 kilobars, Part II, *J. geophys. Res.,* **66,** 2199–2244.

Bird, P., 2002. Stress direction history of the western United States and Mexico since 85 Ma, *Tectonics,* **21,** 1014, doi:10.1019/2001TC001319.

Borradaile, G.J., 1988. Magnetic susceptibility, petrofabrics and strain, *Tectonophysics,* **156,** 1–20.

Borradaile, G.J., 1991. Correlation of strain with anisotropy of magnetic susceptibility (AMS), *Pure appl. Geophys.,* **135,** 15–29.

Borradaile, G.J., 2003. *Statistics of Earth Science Data*, Springer-Verlag, Berlin, Heidelberg and New York, 351 pp., 177 illus., 52 Tables, hardcover ISBN: 3-540-43603-0.

Borradaile, G.J. & Gauthier, D., 2003. Interpreting anomalous magnetic fabrics in ophiolite dikes, *J. Struct. Geol.,* **25,** 171–182.

Borradaile, G.J. & Henry, B., 1997. Tectonic applications of magnetic susceptibility and its anisotropy, *Earth Sci. Rev.,* **42,** 49–93.

Borradaile, G. & Tarling, D.H., 1981. The influence of deformation mechanisms on magnetic fabric in weakly deformed rocks, *Tectonophysics,* **77,** 151–168.

Burmeister, K.C., Harrison, M.J., Marshak, S., Ferré, E.C., Bannister, R.A. & Kodama, K.P., 2009. Comparison of Fry strain ellipse and AMS ellipsoid trends to tectonic fabric trends in very low-strain sandstone of the Appalachian fold–thrust belt, *J. Struct. Geol.,* **31,** 1028–1038.

Callot, J.P. & Guichet, X., 2003. Rock texture and magnetic lineation in dykes, a simple analytical model, *Tectonophysics,* **366,** 207–222.

Chester, J.S. & Chester, F.M., 1990. Fault-propagation folds above thrusts with constant dip, *J. Struct. Geol.,* **12,** 903–910.

Dahlstrom, C.D.A., 1969. Balanced cross sections, *Can. J. Earth Sci.,* **6,** 743–757.

Dickinson, W.R. & Snyder, W.S., 1978. Plate tectonics of the Laramide orogeny, *Geol. Soc. Am. Mem.,* **151,** 355–366.

Dunne, W.M., Onasch, C.M. & Williams, R.T., 1990. The problem of strain-marker centers and the Fry method, *J. Struct. Geol.,* **12,** 933–938.

Dvorkin, J. & Nur, A., 1996. Elasticity of high-porosity sandstones: theory for two North Sea datasets, *Geophysics,* **61,** 1363–1370.

Engebretson, D.C., Cox, A. & Gordon, R.G., 1985. Relative motion between oceanic and continental plates in the Pacific basin, *Geol. Soc. Am.* Special Paper 206, 59 pp.

Erslev, E.A., 1988. Normalized center-to-center strain analysis of packed aggregates, *J. Struct. Geol.,* **10,** 201–209.

Erslev, E.A., 1991. Trishear fault-propagation folding, *Geology,* **19,** 617–620.

Erslev, E.A., 1993. Thrusts, back-thrusts and detachment of Rocky Mountain foreland arches, in *Laramide Basement Deformation in the Rocky Mountain Foreland of the Western United States*, Geol. Soc. Amer. Special Paper **280,** pp. 339–358, eds Schmidt, C.J., Chase, R.B., and Erslev, E.A., Geol. Soc. America, Boulder, CO.

Eshelby, J., 1957. The determination of the elastic field of an ellipsoidal inclusion and related problems, *Proc. Roy. Soc. A,* **241, 1226,** 376–396.

Etchecopar, A., 1984. Etude des états de contraintes en tectonique cassante et simulation de déformations plastiques (approche mathématique), *Ph.D. thesis*. Univ. Sciences et Techniques du Languedoc, Montpellier, 270 pp.

Evans, M.A. & Elmore, R.D., 2006. Corrigendum to: Fluid control of localized mineral domains in limestone pressure solution structures, *J. Struct. Geol.,* **28,** 284–301.

Evans, M.A., Lewchuk, M.T. & Elmore, R.D., 2003. Strain partitioning of deformation mechanisms in limestones: examining the relationship of strain and anisotropy of magnetic susceptibility (AMS), *J. Struct. Geol.,* **25,** 1525–1549.

Fiore, P.E., 2006. 3D characterization and mechanics of brittle deformation in thrust fault related folds, *Ph.D. thesis*. Stanford University, California, USA.

Forster, A., Irmen, A.P. & Vondra, C., 1996. Structural interpretation of Sheep Mountain Anticline, Bighorn Basin, Wyoming, *Wyoming Geol. Assoc. Guidebook,* **47,** 239–251.

Frizon de Lamotte, D., Mercier, E., Dupré la Tour, A., Robion, P. & Averbuch, O., 1997. Cinématique du plissement et déformation interne des roches; l'exemple du pli de Lagrasse (Aude France), *C. R. Acad. Sci., Paris* **324,** 591–598.

Frizon de Lamotte, D., Souque, C., Grelaud, S. & Robion, P., 2002. Early record of tectonic magnetic fabric during inversion of a sedimentary basin. Short review and examples from the Corbières transfer zone (France), *Bull. Soc. Géol. Fr.,* **175,** 461–469.

Fry, N., 1979. Random point distributions and strain measurement in rocks, *Tectonophysics,* **60,** 89–105.

Fuller, M.D., 1964. On the magnetic fabrics of certain rocks, *J. Geol.,* **72,** 368–376.

Graham, J.W., 1966. Significance of magnetic anisotropy in Appalachian sedimentary rocks, in *The Earth Beneath the Continents*, Geophys. Monograph **10,** pp. 627– 648, eds Steinhart, J.S. and Smith, T.J. Am. geophys. Un., Washington.

Graham, W.B.R., 2006. Influence of depositional setting and sedimentary fabric on mechanical layer evolution in carbonate aquifers, *Sed. Geol.,* **184,** 203–224.

Groshong, R.H., 1972. Strain calculated from twinning in calcite, *Geol. Soc. Am. Bull.,* **83,** 2025–2048.

Groshong, R.H., 1974. Experimental test of least-squares strain gage calculation using twinned calcite, *Geol. Soc. Am. Bull.,* **85,** 1855–1864.

Hennier, J. & Spang, J., 1983. Mechanisms for deformation of sedimentary strata at Sheep Mountain anticline, Big Horn Basin, Wyoming, in *Proceedings of the 34th Annual Field Conference*, Wyoming Geological Association Guidebook, pp. 97–111.

Henry, B., 1997, The magnetic zone axis: a new element of magnetic fabric for the interpretation of magnetic lineation, *Tectonophysics,* **271,** 325–331.

Housen, B.A., Richter, C. & Van Der Pluijm, B.A., 1993. Composite magnetic anisotropy fabrics: experiments, numerical models and implications for the quantification of rock fabrics, *Tectonophysics,* **220,** 1–12.

Hrouda, F., 1986. The effect of quartz on the magnetic anisotropy of quartzite, *Stud. Geophys. Geodet.,* **30,** 39–45.

Hrouda, F., 1991. Models of magnetic anisotropy variations in sedimentary thrust sheets, *Tectonophysics,* **185,** 203–210.

Hrouda, F., 2004. Problems in interpreting AMS parameters in diamagnetic rocks, in *Magnetic Fabric, Methods and Applications*, Special Publications **238,** pp. 49–59, eds Martin-Hernadez, F., Lüneburg, C., Aubourg, C. and Jackson, M., Geological Society, London.

Hrouda, F. & Jezek, J., 1999. Theoretical models for the relationship between magnetic anisotropy and strain: effect of triaxial magnetic grains, *Tectonophysics,* **301,** 183–190.

Jamison, W.R., 1987. Geometric analysis of fold development in overthrust terranes, *J. Struct. Geol.* **9**(2), 207–219.

Jelinek, V., 1978. Statistical processing of anisotropy of magnetic susceptibility measured on group of specimens, *Stud. geophys. Geodet.,* **22,** 50–62.

Jelinek, V., 1981. Characterization of the magnetic fabric of the rocks, *Tectonophysics,* **79,** 63–67.

Kachanov, M., 1992. Effective elastic properties of cracked solids: critical review of some basis concepts, *Appl. Mech. Rev.,* **45**(8), 304–335.

Kachanov, M., 1993. Elastic solids with many cracks and related problems, *Adv. Appl. Mech.,* **30,** 259–445.

Kern, H., Liu, B. & Popp, T., 1997. Relationship between anisotropy of P- and S-wave velocities and anisotropy of attenuation in serpentinite and amphibolite, *J. geophys. Res.,* **102**(B2), 3051–3065.

King, M.S., 1965. Wave velocities in rocks as a function of changes in overburden pressure and pore fluid saturants, *Geophysics,* **31,** 50–73.

Kissel, C., Barrier, E., Laj, C. & Lee, T-Q., 1986, Magnetic fabric in «undeformed» Marin clays from compressional zones, *Tectonics,* **5,** 769–781.

Kligfield, R., Lowrie, W. & Dalziel, I.W.D., 1977. Magnetic susceptibility anisotropy as a strain indicator in the sudbury bassin, Ontario, *Tectonophysics,* **40,** 287–308.

Lacombe, O., 2001. Paleostress magnitudes associated with development of mountain belts: Insights from tectonic analyses of calcite twins in the Taiwan Foothills, *Tectonics,* **20**(6), 834–849.

Lacombe, O., 2007. Comparison of paleostress magnitudes from calcite twins with contemporary stress magnitudes and frictional sliding criteria in the continental crust: Mechanical implications, *J. Struct. Geol.,* **29,** 86–99, doi:10.1016/j.jsg.2006.08.009.

Lacombe, O., Amrouch, K., Mouthereau, F. & et Dissez, L., 2007, Calcite twinning constraints on late Neogene stress patterns and deformation mechanisms in the active Zagros collision belt. *Geology,* **35**(3), 263–266, doi:10.1130/G23173A.1.

Lacombe, O., Malandain, J., Vilasi, N., Amrouch, K. & et Roure, F., 2009, From paleostresses to paleoburial in fold-thrust belts: preliminary results from calcite twin analysis in the outer Albanides, *Tectonophysics,* **475,** 128–141, doi:10.1016/j.tecto.2008.10.023.

Ladd, R.E., 1979, The geology of Sheep Canyon Quadrangle: Wyoming, *PhD thesis,* Iowa State University.

Latta, D.K. & Anastasio, D.J., 2007. Multiple scales of mechanical stratification and décollement fold kinematics, Sierra Madre Oriental foreland, northeast Mexico, *J. Struct. Geol.,* **29,** 1241–1255.

Laurent, P., 1984. Les macles de la calcite en tectonique : nouvelles méthodes dynamiques et premières applications. *Thèse de Doctorat-ès-Sciences*. Univ. Sciences et Techniques du Languedoc, Montpellier, 324 pp.

Lo, T.-W., Coyner, K.B. & Toksöz, M.N., 1986. Experimental determination of elastic anisotropy of Berea Sandstone, Chicopee shale, and Chelmsford granite, *Geophysics,* **51,** 164–171.

Louis, L., David, C. & Robion, P., 2003. Comparison of the anisotropic behaviour of undeformed sandstones under dry and saturated conditions, *Tectonophysics,* **370,** 193–212.

Louis, L., Robion, P. & David, C., 2004. A single method for the inversion of anisotropic data sets with application to structural studies, *J. Struct. Geol.,* **26,** 2065–2072.

Louis, L., David, C., Metz, V., Robion, P., Menendez, B. & Kissel, C., 2005. Microstructural control on the anisotropy of elastic and transport properties in undeformed sandstones, *Int. J. Roc. Mech. Min. Sci.,* **42,** 911–923.

Louis, L., Robion, P., David, C. & Frizon de Lamotte, D., 2006. Multiscale anisotropy controlled by folding: the example of the Chaudrons fold (Corbières, France), *J. Struct. Geol.,* **28,** 549–560.

Lowrie, W., 1990. Identification of ferromagnetic minerals in rock by coercitivity and unblocking temperature properties, *Geophys. Res. Lett.,* **17,** 159–162.

Lowrie, W. & Hirt, A.M., 1987. Anisotropy of magnetic suceptibility in the Scaglia Rossa pelagic limestone, *Earth planet. Sci. Lett.,* **82,** 349–356.

Lüneberg, C.M., Lampert, S.A., Lebit, H.D., Hirt, A.M., Casey, M. & Lowrie, W., 1999. Magnetic anisotropy, rock fabrics and finite strain in deformed sediments of SW Sardinia (Italy), *Tectonophysics,* **307,** 51–74.

Mainprice, D., Barruol, G. & Ben Ismaïl, W., 2000. The seismic anisotropy of the earth's mantle: from single crystal to polycrystal, *Geophys. Monogr.,* **117,** 237–264.

Marfil, R., Caja, M.A., Tsige, M., Al-Aasm, I.S., Martín-Crespo, T. & Salas, R., 2005. Carbonate-cemented stylolites and fractures in the Upper Jurassic limestones of the Eastern Iberian Range, Spain: a record of palaeofluids composition and thermal history, *Sediment. Geol.,* **178**(3–4), 237–257.

Mavko, G., Mukerji, T. & Dvorkin, J., 1998, *The Rock Physics Handbook—Tools for Seismic Analysis in Porous Media*, Cambridge University Press, Cambridge.

Mitra, S., 2003. A unified kinematic model for the evolution of detachment folds, *J. Struct. Geol.,* **25,** 1659–1673.

Nye, J.F., 1957. *The physical Properties of Crystals*, Clarendon Press, Oxford, 322 pp.

Owens, W.H. & et Bamford, D., 1976. Magnetic, seismic, and other anisotropic propreties of rock fabrics, *Phil. Trans. R. Acad. Soc., Lond.,* **283,** 55–68.

Parés, J.M. & Van Der Pluijm, B.A., 2002, Evaluating magnetic lineations (AMS) in deformed rocks, *Tectonophysics,* **350,** 283–298.

Parés, J.M., Van Der Pluijm, B.A. & Dinarès-Turell, J., 1999. Evolution of magnetic fabrics during incipient deformation of mudrocks (Pyrenees, northern Spain), *Tectonophysics,* **307,** 1–14.

Paterson, S.R. & Yu, H., 1994. Primary fabric ellipsoids in sandstones; implications for depositional processes and strain analysis, *J. Struct. Geol.,* **16,** 505–517.

Rathore, J.S., 1979. Magnetic susceptibility anisotropy in the Cambrian slate belt of North Wales and correlation with strain, *Tectonophysics,* **53,** 83–97.

Rathore, J., Fjaer, E., Holt, R. & Renlie, L., 1994. P- and S-wave anisotropy of a synthetic sandstone with controlled crack geometry, *Geophys. Prospect.,* **43,** 711–728.

Rioux, R.L., 1994. Geologic map of the Sheep Mountain-Little Sheep Mountain area, Big Horn County, Wyoming. *Scale* **1**(31), 680. USGS open-file report, 94–191.

Rochette, P., 1987. Magnetic susceptibility of the rock matrix related to magnetic fabric studies, *J. Struct. Geol.,* **9**(8), 1015–1020.

Rochette, P., Jackson, J. & Aubourg, C., 1992. Rock magnetism and the interpretation of anisotropy of magnetic susceptibility, *Rev. Geophys.,* **30,** 209–226.

Robion, P., Grelaud, S. & Frizon de Lamotte, D., 2007. Pre-folding magnetic fabrics in fold-and-thrust belts: Why the apparent internal deformation of the sedimentary rocks from the Minervois basin (NE — Pyrenees, France) is so high compared to the Potwar basin (SW — Himalaya, Pakistan)?, *Sed. Geol.,* **196,** 181–200.

Roure, F., *et al*. 2005, Incidence and importance of tectonics and natural fluid migration on reservoir evolution in foreland fold-and-thrust belt, *Oil Gas Sci. Tech.,* **60,** 67–106.

Sagnotti, L., Sperenza, F., Winkler, A., Mattei, M. & Funiciello, R., 1998. Magnetic fabric of clay sediments from the external northern Apennines (Italy), *Phys. Earth planet. Int.,* **105,** 73–93.

Saint-Bezar, B., Hebert, R.L., Aubourg, C., Robion, P., Swenen, R. & Frizon de Lamotte, D., 2002. Magnetic Fabric and petrographic investigations of hematite-bearing sandstones within ramp-related folds: examples from the South Atlas Front (Morocco), *J. Struct. Geol.,* **24,** 1507–1520.

Sans, M., *et al*. 2003. Layer parallel shortening in salt-detached folds: constraint on cross-section restoration, *Tectonophysics,* **372,** 85–104.

Sanz, P.F., Pollard, D.D., Allwardt, P.F. & Borja, R.I., 2008. Mechanical models of fracture reactivation and slip on bedding surfaces during folding of the asymmetric anticline at Sheep Mountain, Wyoming, *J. Struct. Geol.,* **30,** 1177–1191.

Schmidt, V., Günther, D. & et Hirt, A.M., 2006. Magnetic anisotropy of calcite at room-temperature, *Tectonophysics,* **418,** 63–73.

Soto, R., Larrasoaña, J.C., Arlegui, L.E., Beamud, E., Oliva-Urcia, B. & Simón, J.L., 2009. Reliability of magnetic fabric of weakly deformed mudrocks as a palaeostress indicator in compressive settings, *J. Struct. Geol.,* **31**(5), 512–522.

Souque, C., Frizon de Lamotte, D., Leturmy, P. & Robion, P., 2003. Duplex at the lateral tip of a thrust fault: the "La Cagalière" example (NE Pyrenees, France), *Geodinamica Acta,* **16**(2), 89–98.

Stanton, H.I. & Erslev, E.A., 2004. Sheep Mountain Anticline: backlimb tightening and sequential deformation in the Bighorn Basin, Wyoming, *Wyoming Geol. Assoc. Guidebook,* **53,** 75–87.

Suppe, J., 1985. *Principles of Structural Geology*, Prentice-Hall, Englewood Cliffs, NJ, 537 pp.

Thomsen, L., 1986. Weak elastic anisotropy, *Geophysics,* **51,** 1954–1966.

Tsvankin, I., 1997. Anisotropic parameters and P-wave velocity for orthorhombic media, *Geophysics,* **62,** 1292–1309.

Wetmore, P.H., 2003. Investigation into the Tectonic Significance of Along Strike Variations of the Peninsular Ranges batholith, Southern and Baja California. *PhD thesis*. University of Southern California.